P926

Measurement of $K_L^0 \to \pi^0 \nu \bar{\nu}$

I-Hung Chiang, J. W. Glenn, Donald Lazarus,
Laurence Littenberg, Richard Strand, Craig Woody
Brookhaven National Laboratory
Dmitri Dementyev, Alexandr Ivashkin, Alexei Khotjanzev,
Yury Kudenko, Oleg Mineev
INR, Moscow
Hisaya Kurashige, Noboru Sasao
Kyoto University
James Lowe, Bernd Bassalleck
University of New Mexico
Mark Ito
Thomas Jefferson National Accelerator Facility
Ewart Blackmore, Douglas Bryman, Peter Gumplinger,
Michael Hasinoff, Akira Konaka, John Macdonald,
Toshio Numao, Renée Poutissou, Gregory Smith
TRIUMF
Marvin Blecher, Kay Kinoshita
Physics Department, Virginia Polytechnic Institute
Satish Dhawan, Heinz Kaspar, Walid Majid,
Michael Zeller
Physics Department, Yale University

September 4, 1996

Abstract

A proposed measurement of the rare decay $K_L \rightarrow \pi^0 \nu\bar{\nu}$ is described. The method employs kaon time-of-flight and full kinematic reconstruction of the π^0 to suppress backgrounds to a level well below an anticipated signal in the range $3 \pm 2 \times 10^{-11}$.

Contents

List of Figures

List of Tables

1 $K_L \to \pi^0 \nu\bar{\nu}$ – Theoretical Motivation

1.1 Standard Model

Understanding the phenomenology of quark mixing and CP violation is currently one of the central goals of particle physics. Examining the CKM ansatz of the Standard Model (SM) through precise determination of its basic parameters, several of which are poorly known at present, is crucial. To assure a clear interpretation of experimental results, the ideal observable must not only be sensitive to fundamental parameters, but must also be calculable with small theoretical ambiguity.

The rare decay $K_L \to \pi^0 \nu\bar{\nu}$ is unique among potential SM observables; it is dominated by direct CP violation [1] and is entirely governed by short-distance physics involving the top quark (for general reviews see [2]). Theoretical uncertainties are extremely small because the hadronic matrix element can be extracted from the well measured decay $K^+ \to \pi^0 e^+ \nu$, where small isospin breaking effects have been calculated. Since the dominant uncertainty due to renormalization scale dependence has been practically eliminated by including next-to-leading QCD corrections, the remaining theoretical uncertainty for $B(K_L \to \pi^0 \nu\bar{\nu})$ is reduced to O(1%).

$K_L \to \pi^0 \nu\bar{\nu}$ is a flavor-changing neutral current (FCNC) process that is induced through loop effects in the Standard Model. The leading electroweak diagrams are shown in fig. 1. The expression for the $K_L \to \pi^0 \nu\bar{\nu}$ branching

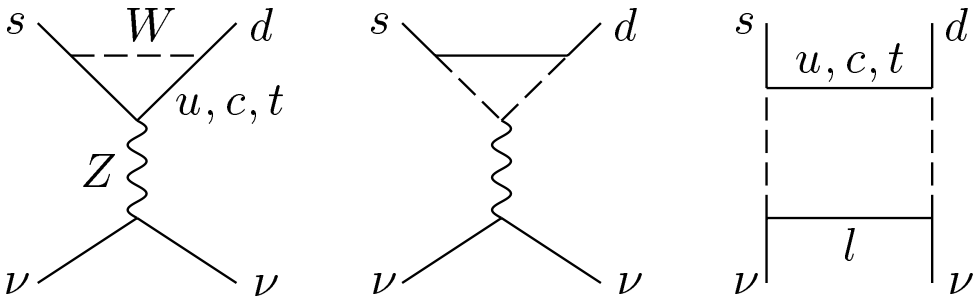

Figure 1: The leading electroweak diagrams inducing $K_L \to \pi^0 \nu\bar{\nu}$.

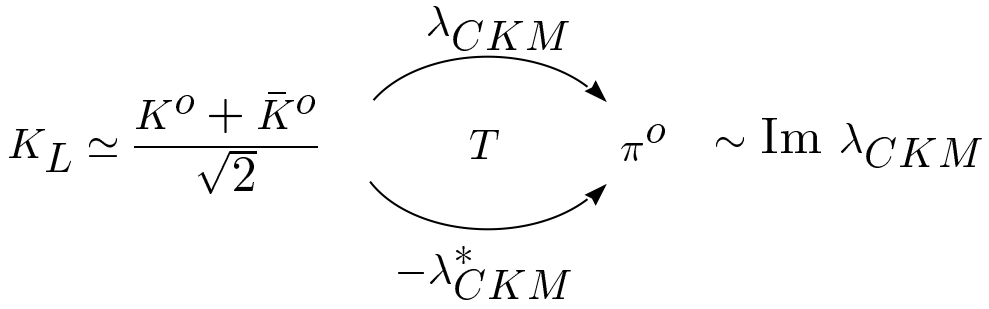

Figure 2: Direct CP violation in $K_L \to \pi^0 \nu\bar{\nu}$. K_L decays into π^0 by means of the transition current $T = \lambda_{CKM}(\bar{s}d)_V + \lambda^*_{CKM}(\bar{d}s)_V$. The CP transformation properties are $CP\ K^0 = -\bar{K}^0$, $CP\ \pi^0 = -\pi^0$ and $CP(\bar{d}s)_V CP^{-1} = -(\bar{s}d)_V$.

ratio can be written as

$$B(K_L \to \pi^0 \nu\bar{\nu}) = r_{IB} B(K^+ \to \pi^0 e^+ \nu) \frac{\tau(K_L)}{\tau(K^+)} \frac{3\alpha^2}{2\pi^2 \sin^4 \Theta_W} \eta^2 A^4 \lambda^8 X^2(x_t) \tag{1}$$

where

$$X(x) = \eta_X \cdot \frac{x}{8}\left[\frac{x+2}{x-1} + \frac{3x-6}{(x-1)^2}\ln x\right] \qquad \eta_X = 0.985 \tag{2}$$

and $x_t = m_t^2/M_W^2$. Here the appropriate top quark mass to be used is the running $\overline{MS}$ mass, $m_t \equiv \bar{m}_t(m_t)$, which is related by $\bar{m}_t(m_t) = m_t^*(1 - 4/3 \cdot \alpha_s(m_t)/\pi)$ to the pole mass m_t^* measured in collider experiments. With this choice of mass definition the QCD correction factor is given by $\eta_X = 0.985$ and essentially independent of m_t [3]. The coefficient $r_{IB} = 0.944$ summarizes the leading isospin breaking corrections in relating $K_L \to \pi^0 \nu\bar{\nu}$ to $K^+ \to \pi^0 e^+ \nu$ [4].

$K_L \to \pi^0 \nu\bar{\nu}$ is driven by direct CP violation due to the CP properties of K_L, π^0 and the relevant short-distance hadronic transition current. Since K_L is predominantly a coherent, CP odd superposition of K^0 and $\bar{K}^0$, only the imaginary part of $V_{td} \sim \eta$ survives in the amplitude, as illustrated in fig. 2. As a consequence $B(K_L \to \pi^0 \nu\bar{\nu}) \sim \eta^2$ (eqn. 1). Using current estimates

for SM parameters, the branching ratio for $K_L^0 \to \pi^0 \nu\bar{\nu}$ is expected to lie in the range of about $(3 \pm 2) \cdot 10^{-11}$.

We have employed the Wolfenstein parametrization (λ, A, ϱ, η) of the CKM matrix, which allows a display of unitarity in a transparent way. The Wolfenstein parameters may be defined by

$$V_{us} = \lambda \qquad V_{cb} = A\lambda^2 \qquad V_{ub} = A\lambda^3(\varrho - i\eta) \tag{3}$$

While A, ϱ, η are treated as quantities of order one, the sine of the Cabibbo angle $V_{us} = \lambda = 0.22$ is a small number that can be used as an expansion parameter. The unitarity relation

$$1 + \frac{V_{td}V_{tb}^*}{V_{cd}V_{cb}^*} = -\frac{V_{ud}V_{ub}^*}{V_{cd}V_{cb}^*} \equiv \bar{\varrho} + i\bar{\eta} \tag{4}$$

determines a triangle in the $(\bar{\varrho}, \bar{\eta})$ plane. Here $\bar{\varrho} = \varrho(1 - \lambda^2/2)$ and $\bar{\eta} = \eta(1 - \lambda^2/2)$ to an accuracy of better than 0.1%. This unitarity triangle is illustrated in fig. 3. A clean measure of its height is provided by the $K_L \to \pi^0 \nu\bar{\nu}$ branching ratio.

The charged mode $K^+ \to \pi^+ \nu\bar{\nu}$ is closely related to $K_L \to \pi^0 \nu\bar{\nu}$. However, it is not CP violating and receives a non-negligible charm contribution leading to a slightly higher theoretical uncertainty (about 5%) [5]. Measurement of $B(K^+ \to \pi^+ \nu\bar{\nu})$ allows the extraction of $|V_{td}|$ with the least theoretical uncertainty. Together with $B(K_L \to \pi^0 \nu\bar{\nu})$ the unitarity triangle is completely determined as shown in fig. 3. Only a few other possible SM observables (e.g. x_s/x_d, $B \to l^+l^-$ or certain CP asymmetries in B decays) provide similar opportunities for unambiguously revealing SM effects.

To illustrate the phenomenological potential of $B(K_L \to \pi^0 \nu\bar{\nu})$ we briefly discuss a few conceivable applications of a branching ratio measurement. Of the four independent CKM parameters λ, A, ϱ and η, λ is measured in $K \to \pi e \nu$ and $A = V_{cb}/\lambda^2$ can be extracted from $B \to D^* e\nu$ or inclusive semileptonic B decay. Two of the most important channels that will be studied at the B factories and elsewhere are B^0 or $\bar{B}^0 \to \pi\pi$ and B^0 or $\bar{B}^0 \to J/\psi K_S$. At B factories the time-dependent asymmetry in the rate between B^0 and $\bar{B}^0$ must be measured in both cases. These CP violating asymmetries measure $\sin 2\alpha$ and $\sin 2\beta$, respectively, and could be used to infer ϱ and η (fig. 3), completing the CKM determination.

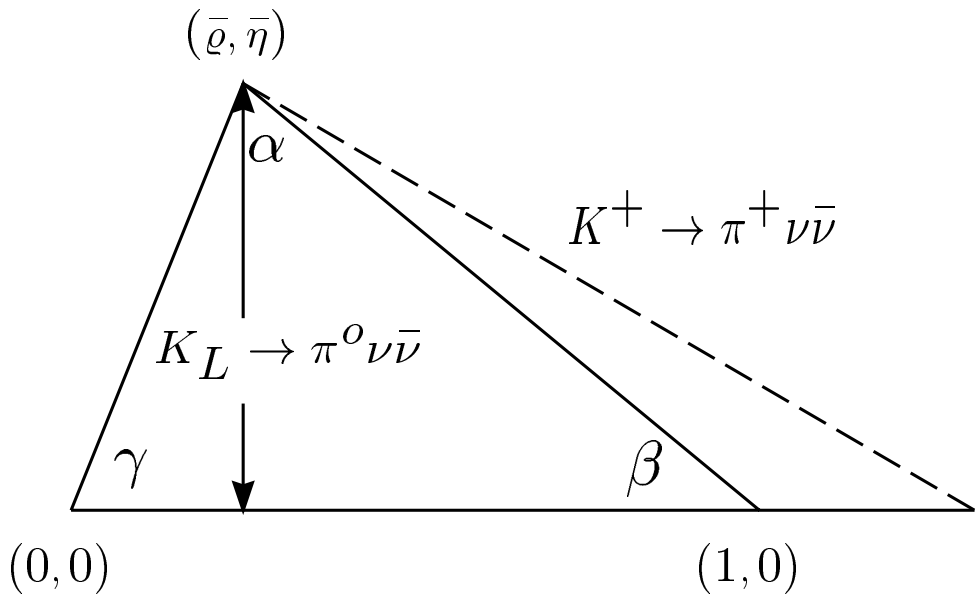

Figure 3: The unitarity triangle.

As an alternative, ϱ and η can be obtained from the two $K \to \pi\nu\bar{\nu}$ decay modes as seen in fig. 3. A comparison of both strategies is displayed in Table 1 (see also [6]), where, as an example, the following input has been used

$$V_{cb} = 0.040 \pm 0.002 \qquad m_t = (170 \pm 3) GeV \tag{5}$$

$$B(K_L \to \pi^0 \nu\bar{\nu}) = (3.0 \pm 0.3) \cdot 10^{-11} \qquad B(K^+ \to \pi^+ \nu\bar{\nu}) = (1.0 \pm 0.1) \cdot 10^{-10} \tag{6}$$

The charm contribution in $K^+ \to \pi^+ \nu\bar{\nu}$ is assumed to be known to $\pm 15\%$. The measurements of CP asymmetries in $B_d \to \pi\pi$ and $B_d \to J\psi K_S$, expressed in terms of $\sin 2\alpha$ and $\sin 2\beta$, are taken to be

$$\sin 2\alpha = 0.40 \pm 0.10 \qquad \sin 2\beta = 0.60 \pm 0.06 \tag{7}$$

which corresponds to the accuracy being aimed for at B-factories prior to the LHC era.

	$\sin 2\beta$	$\bar{\eta}$	$\bar{\varrho}$	$\lvert V_{td}\rvert/10^{-3}$
$K \to \pi\nu\bar{\nu}$	0.62 ± 0.05	0.38 ± 0.04	-0.10 ± 0.16	10.3 ± 1.1
$B \to \pi\pi, J/\psi K_S$	0.60 ± 0.06	0.32 ± 0.04	0.04 ± 0.02	8.9 ± 0.5

Table 1: Illustrative example of the determination of CKM parameters from $K \to \pi\nu\bar{\nu}$ and from CP violating asymmetries in B decays. The relevant input is as described in the text.

As can be seen from Table 1, the determination of CKM parameters from $K \to \pi\nu\bar{\nu}$ is comparable to the one possible with CP asymmetries in B decays, with the exception of $\bar{\varrho}$. However, the extraction of $\sin 2\alpha$ from $B \to \pi\pi$ is complicated by the presence of penguin contributions. If only the channel $B_d \to \pi^+\pi^-$ is used, these contributions introduce potentially sizable theoretical uncertainties [7]. On the other hand, avoiding penguin effects requires a careful isospin analysis and a combination of several modes, including the challenging decay $B_d \to \pi^0\pi^0$. Also, inferring $\bar{\varrho}$ and $\bar{\eta}$ from $\sin 2\alpha$ and $\sin 2\beta$ involves discrete ambiguities, so that some additional information (e.g. on the size of V_{ub}) is necessary to single out a unique solution. The CKM analysis for $K \to \pi\nu\bar{\nu}$ is less complicated, which could turn out to be of advantage in the unitarity triangle determination. We finally note that in Table 1 the error on $\bar{\eta}$ from $K_L \to \pi^0\nu\bar{\nu}$ can be further reduced by lowering the uncertainty in V_{cb}. It would decrease to below ± 0.03 if $\Delta V_{cb} = \pm 0.001$.

Alternatively, results from the CP violation experiments in B physics and a $K_L \to \pi^0\nu\bar{\nu}$ measurement could also be combined for high precision determinations of the CKM matrix. In a scenario proposed in [8], λ would be derived from $K \to \pi e\nu$ as usual, while $B_d \to \pi\pi$ and $B_d \to J/\psi K_S$ could give ρ and η. Then, knowing η, $K_L \to \pi^0\nu\bar{\nu}$ should allow a very accurate determination of A, taking advantage of the fact that A depends only rather weakly upon $B(K_L \to \pi^0\nu\bar{\nu})$, $A \sim [B(K_L \to \pi^0\nu\bar{\nu})]^{1/4}$ (1). This step would complete a CKM matrix determination that is essentially free of hadronic uncertainties. The method could become interesting in particular when CP asymmetries in B decays will be measured with improved precision at the LHC. As an example we assume $\sin 2\alpha = 0.40 \pm 0.04$, $\sin 2\beta = 0.60 \pm 0.02$

and $B(K_L \to \pi^0 \nu\bar{\nu}) = (3.0 \pm 0.3) \cdot 10^{-11}$, $m_t = (170 \pm 3) GeV$. This yields [6]

$$\bar{\varrho} = 0.04 \pm 0.01 \quad \bar{\eta} = 0.32 \pm 0.01 \quad |V_{cb}| = 0.0428 \pm 0.0014 \tag{8}$$

Such a precise determination of the independent CKM parameters, in which $K_L \to \pi^0 \nu\bar{\nu}$ plays a crucial role, would provide an ideal basis for comparison with other observables sensitive to mixing angles, like $K^+ \to \pi^+ \nu\bar{\nu}$, $B \to \pi l \nu$, x_s/x_d or V_{cb} from $b \to c$ transitions. Any additional, independent determination of CKM parameters would then constitute a test of the Standard Model. Any significant deviation would point to new physics.

1.2 Non-standard Models

Extensions of the Standard Model can in principle modify the physics discussed above in many ways. Usually extended models introduce a variety of new degrees of freedom and a priori unknown parameters, and it is therefore difficult to obtain definite predictions. We would however like to make a few general remarks relevant for $K_L \to \pi^0 \nu\bar{\nu}$ and the comparison with CP asymmetries in B decays. For a review of CP violation in B physics beyond the SM see [9].

A clean SM test is provided by comparing η as determined from $B \to \pi\pi$ and $B \to J/\psi K_S$ with η from $K_L \to \pi^0 \nu\bar{\nu}$. A discrepancy would clearly indicate new physics. The theoretical precision of the observables under discussion is crucial as the deviation might not be very large.

Next, a measurement of CP asymmetries in $B \to \pi\pi$, $B \to J/\psi K_S$ would still be consistent with superweak theories if $\sin 2\alpha$ turned out to coincide with $-\sin 2\beta$. On the other hand, just establishing a non-zero $B(K_L \to \pi^0 \nu\bar{\nu})$ rules out a pure superweak explanation of CP violation.

Furthermore, in some new physics scenarios, as multi-Higgs doublet models or minimal SUSY in which the CKM matrix remains the sole source of CP violation, the extraction of $\sin 2\alpha$ and $\sin 2\beta$ from CP asymmetries in B decays would be unaffected. Such effects might then show up in a comparison with $K_L \to \pi^0 \nu\bar{\nu}$, where e.g. charged Higgs contributions modify the top quark dependent function $X(x_t)$ in (1).

In [10, 11] the decay $K_L \to \pi^0 \nu\bar{\nu}$ has been studied within the framework of extended Higgs models. The simplest possibility is a two-Higgs doublet model with natural flavor conservation. In this model CP violation still

originates entirely from the CKM matrix. Constraints derived from existing measurements of CP violation in $K \to \pi\pi$ (ε_K), $B - \bar{B}$ mixing and $b \to s\gamma$ decay are known to restrict the allowed parameter space ($\tan\beta$, $M_{H^\pm}$) substantially. In spite of this, the $K_L \to \pi^0\nu\bar{\nu}$ branching ratio could still exceed the SM expectation by $\sim 50\%$ if $\tan\beta \sim 1$. This result should also be indicative for models like minimal SUSY, where the additional contributions are also constrained by data on the above mentioned observables. In the related case of $K^+ \to \pi^+\nu\bar{\nu}$ this has been demonstrated in [12], where several SM extensions such as minimal SUSY, fourth-generation and left-right symmetric models were analyzed. The general conclusion to be drawn from this investigation was that these more conventional extensions do not allow too dramatic deviations from the SM result for $K^+ \to \pi^+\nu\bar{\nu}$ once the known experimental constraints are imposed. Large deviations could not be excluded only in some more exotic models, typically involving tree-level FCNC. A similar behavior can be expected for $K_L \to \pi^0\nu\bar{\nu}$ as well.

Examples for new physics scenarios that show drastic deviations from the Standard Model are provided by some of the extended Higgs models discussed in [11]. Specifically in theories where CP violation arises predominantly from the Higgs sector, as in the two-doublet model of spontaneous CP violation of Liu and Wolfenstein and in the three-doublet model due to Weinberg, it was found that $B(K_L \to \pi^0\nu\bar{\nu})$ would be much smaller than in the Standard Model after inclusion of the ε_K constraint. A measurement of $K_L \to \pi^0\nu\bar{\nu}$ at the SM level would thus severely constrain those types of new physics scenarios.

1.3 Theoretical summary

As a consequence of unprecedented theoretical precision and anticipated experimental accessibility, a measurement of $K_L^0 \to \pi^0\nu\bar{\nu}$ can unambiguously test the SM origin of CP violation and ultimately yield the most accurate determination of the CKM CP violating phase η. This rare decay mode therefore provides an exceptional and unique opportunity for making significant progress in our understanding of flavor-dynamics and CP violation. It is competitive with and complementary to future measurements in the B meson system. Absence of $K_L^0 \to \pi^0\nu\bar{\nu}$ within the expected range of about $(3 \pm 2) \cdot 10^{-11}$ or a conflict with other CKM determinations would certainly indicate new physics.

2 The $K_L^0 \rightarrow \pi^0\nu\bar{\nu}$ Experiment

2.1 Introduction

The signature of the $K_L^0 \rightarrow \pi^0\nu\bar{\nu}$ decay mode involves exactly two photons whose invariant mass is consistent with that of a π^0, and nothing else. The difficulty of positively identifying $K_L^0 \rightarrow \pi^0\nu\bar{\nu}$ stems from the all neutral initial and final states and the fact that the probability that a decaying K_L^0 will emit at least one π^0 is about 0.28 whereas the mode being sought has a decay probability ten orders of magnitude smaller. To make the problem worse, interactions between hadrons in the beam (neutrons and kaons) and residual gas in the decay volume can also cause emission of single π^0s as can the decays of copiously produced lambdas (i.e. $\Lambda \rightarrow \pi^0$n).

For any experiment seeking $\pi^0\nu\bar{\nu}$ the most important means of eliminating unwanted events will be to determine that nothing other than one π^0 was emitted in the decay, *i.e.* to veto any extra particles. The most difficult mode to suppress in this manner is $\mathrm{K}_\mathrm{L}^0 \rightarrow 2\pi^0(K_{\pi 2}^0)$. If this were the only defense against unwanted events, however, an extremely high (perhaps unachievable) photon veto detection efficiency would be required. Although AGS experiment E787 has extensively studied hermetic detector photon detection efficiency, considerable uncertainty exists as to the role of photonuclear processes, making predictions of significant advancement in veto efficiency unreliable. Thus, to increase the probability that the source of observed π^0 plus nothing events is truly the $\pi^0\nu\bar{\nu}$ mode another handle is needed. That handle is found at the AGS: measurement of the decaying K_L^0 momentum using time-of-flight. This measurement is achieved by employing very low momentum kaons and a highly time-structured proton beam. Such a system imposes kinematic constraints allowing event-by-event reconstruction in the K_L^0 center of mass frame which not only aids in rejecting bogus kaon decays, but significantly helps in avoiding other potential backgrounds which would be extremely difficult, if not impossible, to eliminate otherwise. Along with its position as the world's most intense proton synchrotron, the new microbunching capability makes the AGS a uniquely suited facility with which to perform this critically important experiment.

In addition to enhancing the neutral particle momentum resolution attainable via time-of-flight measurements, there are other benefits of working at low, rather than high energies. Among these are that Λs, a serious poten-

tial background source at higher energies, are suppressed to negligible levels because they do not survive to reach the decay volume. In addition, most beam neutrons are too low in energy to produce π^0s and many of those with sufficient energy arrive later than the kaons of interest. In addition, any photons originating in the production target region arrive simultaneously, several ns prior to the fastest kaons. The hypothetical advantage of working at higher energy, improved photon detection efficiency, is greatly overshadowed by the kinematic constraints offered in the low energy regime discussed here.

The goal of this project is to observe and definitively measure the rate of the decay $K_L^0 \to \pi^0\nu\bar{\nu}$. We aim to unambiguously detect a large sample of events so that η, the SM CP violation parameter, can be determined to better than 15% statistical accuracy without serious interference from background or systematic effects. We have scoped the experiment for a sensitivity of approximately 4×10^{-13} allowing for nearly an order of magnitude contingency to meet the goal of a successful measurement. In this report, we demonstrate conceptual technical solutions for the significant challenges presented by the measurement of $K_L^0 \to \pi^0\nu\bar{\nu}$, for the most part involving only minimal extensions of existing technology. Continued evolution of the design of individual components, comprehensive simulations and detailed designs, engineering and prototyping will be pursued.

In the following, we give a brief discussion of previous experiments and techniques followed by an overview of the proposed method. Aspects of the AGS proton beam and targeting, the design of the neutral K beam, the detector and estimates of backgrounds and sensitivity are presented in subsequent chapters.

2.2 Previous experiments and techniques

The first experiment to explicitly search for $K_L^0 \to \pi^0\nu\bar{\nu}$ was done at FNAL[13]. In this work, an upper limit of $< 5.7 \times 10^{-5}$ was reached using the $\pi^0 \to ee\gamma$ Dalitz decay to define a restricted region of transverse momentum (P_t). Although the Dalitz decay has a branching ratio of only 1.2%, its use was effective in the effort to suppress backgrounds from Λ decays and radiative K_{e3} decays at the level of sensitivity sought. Using this technique along with an enhanced photon veto capability and improved triggering, E799 at FNAL aims at a sensitivity of about 10^{-8} where backgrounds

from $K^0_{\pi 2}$ ($K^0_{\pi 2}$ branching ratio of 9×10^{-4}) become important. An experiment was recently proposed at KEK seeking a single event sensitivity of 2×10^{-11} employing a highly collimated "pencil" beam.

In future experiments aiming for a measurement of $K^0_L \to \pi^0 \nu\bar{\nu}$, the dominant source of background is likely to be $K^0_{\pi 2}$ decay in which two photons are missed. The phase space for $K^0_L \to \pi^0 \nu\bar{\nu}$ decay could be restricted to the small P_t region above the $K^0_{\pi 2}$ two-pion center-of-mass momentum (which would be further reduced by resolution effects). However, this limited acceptance approach would still leave the equally serious "odd pairing" background which occurs when one photon from each π^0 is missed or ("hides" within the shower of another) and the remaining pair conspires to mimic a π^0.

The main impediment to fully suppressing $K^0_{\pi 2}$ is imperfect photon detection efficiency. Limitations on achievable detection efficiency have been extensively explored in the AGS experiment E787 for π^0s of 205 MeV/c which have decay photons in the range of 20 to 225 MeV. π^0 inefficiency of approximately 10^{-6} has been demonstrated. It appears that shower leakage and photo-nuclear effects (in which photons interact and "disappear" leaving only invisible energy in the form of neutrons or excited nuclei) result in a finite achievable detection inefficiency even when nearly hermetic coverage is attained or nearly ideal crystal photon detectors are used.

Time-of-flight in neutral kaon experiments was effectively employed in early experiments at electron accelerators like SLAC where the high RF frequencies lead to beam bunches with widths of a few picoseconds and at proton accelerators such as the PPA which had bunched beams. As will be discussed below, the AGS has recently acquired the capability to provide tightly bunched beams.

2.3 Overview of the $K^0_L \to \pi^0 \nu\bar{\nu}$ measurement technique

Since the 3-body π^0 spectrum is the only observable in $K^0_L \to \pi^0 \nu\bar{\nu}$, the most effective strategy for an unambiguous measurement is to fully reconstruct the π^0 in the K_L center of mass frame. This can only be efficiently and unambiguously accomplished by completely measuring the kinematics of the decay photons including time, position, angle and energy and by determining

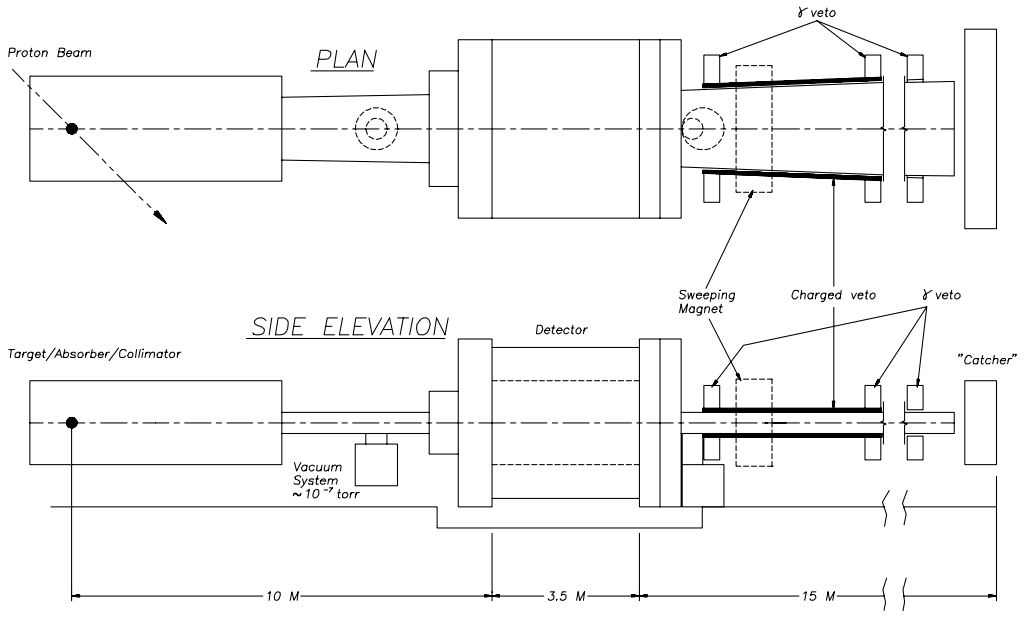

Figure 4: Layout of the $K_L^0 \to \pi^0 \nu \bar{\nu}$ experiment.

the K_L momentum by time-of-flight from the production target. This method results in positive identification of the signal and effective suppression of the background since, for example, the two-body $K_{\pi 2}^0$ decay identifies itself by the unique momentum of the π^0 when viewed in the K_L rest frame. Once the K_L momentum is known, a large fraction of the $K_L^0 \to \pi^0 \nu \bar{\nu}$ phase space is available for detection and all the major sources of background become manageable as discussed below.

Figure 4 shows a schematic of the proposed arrangement of the experiment. A 500 μsr solid angle neutral beam is extracted at 45^o to produce a "soft" K_L spectrum peaked at 0.65 GeV/c; kaons in the range from about 0.5 GeV/c to 1.3 GeV/c will be used. The vertical acceptance of the beam (0.004 r) is kept much smaller than the horizontal acceptance (0.125 r) so that effective collimation can be obtained to severely limit beam halos. Downstream of the final beam collimator is a 3.5 m long decay region which is surrounded by the main detector. Approximately 16% of the kaons decay yielding a decay rate of about 25 MHz. The beam region is evacuated to

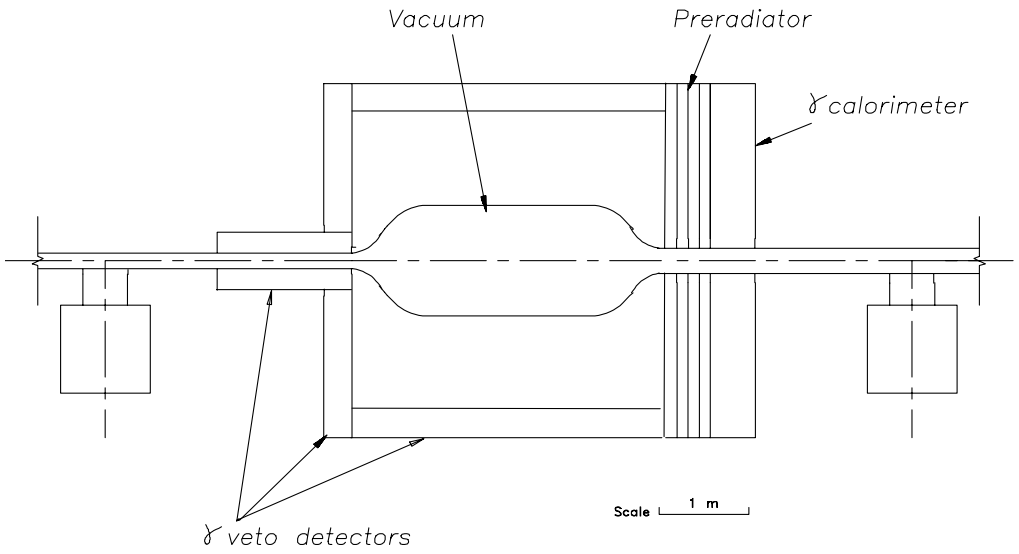

Figure 5: $K_L^0 \to \pi^0 \nu\bar{\nu}$ detector.

a level of 10^{-7} Torr to suppress neutron induced π^0 production. The decay region is surrounded by an efficient Pb/scintillator photon veto detector.

In the forward detection region the primary photon detector system, illustrated in fig. 5, consists of two sections: a fine grained preradiator in which the photons are converted and the first e^+/e^- pair is tracked, followed by a 18 radiation length (X_0) calorimeter in which the remaining energy of the photon shower is measured. The preradiator consists of 42 layers each with plastic scintillator, 0.03 X_0 of heavy metal and dual coordinate drift chambers. The preradiator which has a total effective thickness of 1.5 X_0 functions to measure the photon positions and directions accurately in order to allow reconstruction of the K_L decay vertex while also contributing to the achievement of sufficient energy resolution. The calorimeter is constructed using thin Pb sheets formed to accept scintillating fibers in an arrangement similar to that recently made for the KLOE experiment at DAΦNE; in our implementation of the calorimeter, a significantly higher visible light fraction will be used to further improve the energy resolution. Downstream of the main π^0 detector, a beam hole photon counter consists of Čerenkov detectors designed to be insensitive to neutrons.

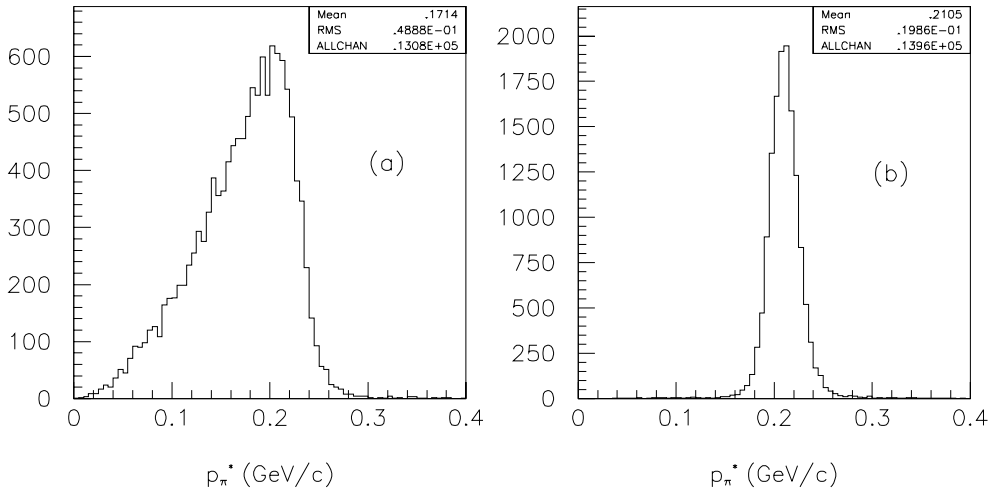

Figure 6: p_π^* distributions using kinematic fitting. (a) $K_L^0 \to \pi^0\nu\bar{\nu}$ and (b) $K_{\pi 2}^0$.

To illustrate how the proposed detector will function to identify the $K_L^0 \to \pi^0\nu\bar{\nu}$ decay and reject backgrounds using the added handle of kinematics, we will consider the background associated with $K_{\pi 2}^0$ when one of the π^0s is missed.[1] Fig. 6 shows the reconstructed momentum of the detected π^0 in the K_L center-of-mass frame (p_π^*) for both $K_L^0 \to \pi^0\nu\bar{\nu}$ signal and the $K_{\pi 2}^0$ background from a Monte Carlo simulation. Resolution in the measured quantities were set to reference values given in Table 2. The histograms include all events where two photons were within the detector's geometric acceptance. The reconstruction included a kinematic fit to reduce the width of the background peak.

Fig. 7 shows the acceptance of a p_π^* cut on the signal and background. A cut with a rejection factor of 50 against the background will have an acceptance of about 35%. When reasonable photon veto efficiency values

[1]The two types of $K_{\pi 2}^0$ backgound are the "even pairing" case when the two observed photons come from one π^0 and the odd pairing case when each photon originates from a different π^0. The odd pairing events will generally not reconstruct to the π^0 mass and are also suppressed by kinematic constraints as will be discussed below.

Quantity	Nominal value	σ used in smearing
E	C_E (0.03 GeV$^{1/2}$)	$C_E/\sqrt{E}$
θ_{xz}	$\sigma_{\theta xz}$ (0.025 radians)	$\sigma_{\theta xz}$
θ_{yz}	$\sigma_{\theta yz}$ (0.025 radians)	$\sigma_{\theta yz}$
x	C_x (0.45 cm-GeV$^{1/2}$)	$C_x/\sqrt{E}$
y	C_y (0.45 cm-GeV$^{1/2}$)	$C_y/\sqrt{E}$
t	σ_t (0.25 ns)	σ_t

Table 2: Nominal smearing parameters and σ's used in the simulation. Each measured quantity was smeared by adding a quantity $G\sigma$ where G is a random value chosen from a normal distribution with zero mean and unit variance, and σ is given in the table.

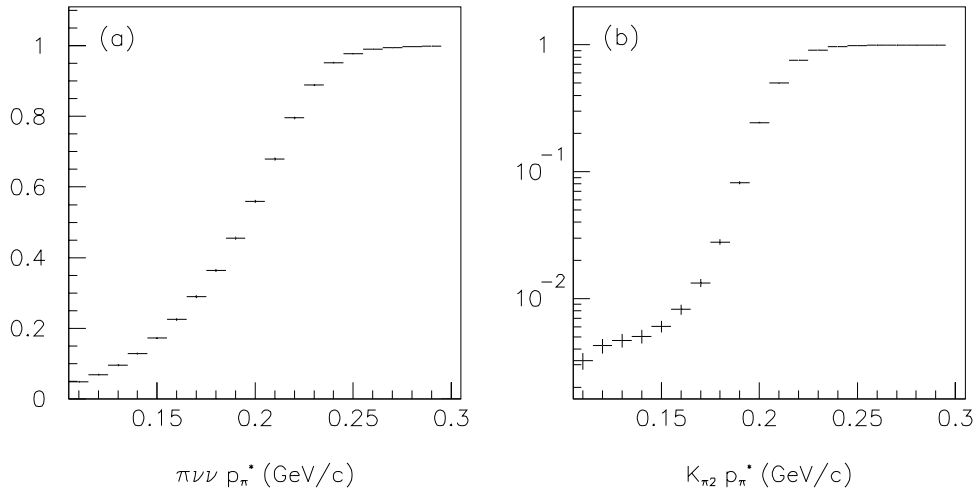

Figure 7: Acceptance vs. p_π^* cut position for (a) $K_L^0 \to \pi^0\nu\bar{\nu}$ and (b) $K_{\pi 2}^0$ (note the logarithmic vertical scale).

based on E787 measurements are also assumed, the added capability of full kinematic reconstruction leads to the $K^0_{\pi 2}$ background being suppressed to a level well below the anticipated signal. A more complete discussion of the potential backgrounds is given below.

3 AGS

3.1 Primary beam luminosity

In recent years the AGS has achieved new records of intensity for synchrotrons. The present SEB peak extraction current of 6×10^{13} protons/pulse (with 1.6 s pulses every 3.6 s) is expected to double by 1999. For estimates here we will assume that 5×10^{13} protons/pulse will be available for K_L production. Coupled with a high current micro-bunched beam, good duty factor and extended availability during the RHIC era,[2] the AGS is the ideal accelerator site for rare neutral kaon decay experiments employing time-of-flight.

3.2 Bunched beam

Short O(100ps) bunches of protons on the kaon production target are desired so that the time-of-flight measurements can result in a few % momentum resolution in the experimental configuration described above. The potential method of keeping the beam bunched in RF buckets and compressing them would require excessive voltage to make the bunches this short. The method[14, 15] chosen here involves the following three steps: 1) With constant field in the main guide magnets, power an RF cavity that creates a string of empty RF longitudinal buckets around the AGS at a radius outside a de-bunched, coasting beam; 2) Set the radius of the extraction transverse resonance at the radius of these empty buckets; and 3) Force the protons in the coasting beam between these buckets by slowly reducing the main guide field. As extraction occurs where the beam is being forced between the separatrix lines of the empty buckets at the point at which they are closest, the

[2] RHIC is projected to operate for 30 to 40 weeks per year and requires injection from the AGS for 2 hours/day. Thus, approximately 22 hours/day are available for AGS proton operation.

extracted beam has the desired structure.

There has been a recent series of tests of this concept at the AGS, exploiting a VHF acceleration cavity that is normally used to dilute the beam in longitudinal space. It operates at about 93 MHz with $\sim$ 30 KV across the gap. For bunched extraction it is powered after the beam is accelerated to full energy and the main field is fixed. This creates 251 empty buckets, every 3.35 m around the AGS, with an energy width of 20 MeV. The guide field is then reduced at a rate of about 0.4%/sec. The resultant stable phase angle is 0.5^o and the gap between buckets is 15^o or 0.5 ns. The frequency of the cavity is also ramped down, since the momentum of the extracted protons is falling with guide field (this frequency change is $\sim$ 1 part in 10^5). The motion through this gap is highly non-linear; tracking of particles in simulations[15] indicate the RMS width of a bunch forced between buckets with this configuration should be $\sim$ 160 ps.

During the 1995 SEB run, an initial test of this concept was carried out using separated K^+'s in the C4 beam line. Signals from a beam Čerenkov counter were timed against the RF acceleration voltage. As the radius and thus frequency of extraction was not directly measured, the frequency was adjusted to minimize bunch width. The minimum achievable bunch width was limited by the beam momentum dispersion and by instrumental resolution, but well-separated bunches of $\sim$ 550 ps were observed. In 1996, test activities were moved to the B2 test beam off the B target where very fast timing counters were available. To avoid the effects of possible momentum dispersion, electrons were selected. In a May test run, bunch widths $<$ 400 ps were achieved. There were some hints that smaller widths were occurring during short periods of the spill, but software problems prevented following this up.

After improvements in the beam line and analysis software, another test was performed in June. The RMS bunch width and phase as a function of frequency from this test is shown in fig. 8. The widths are still somewhat larger than expected. As the beam did not have a uniform distribution in momentum, the momentum did not change linearly in time and the frequency of the cavity with a linear ramp did not correctly track the velocity change of the protons. Measuring the bunch width for 15% of the spill showed a 35% reduction in bunch width. Fig 9 shows the narrowest of these distributions, from which a Gaussian fit extracts an RMS width of $\sim$ 300 ps.

Further progress is expected as the instrumentation and feedback circuitry

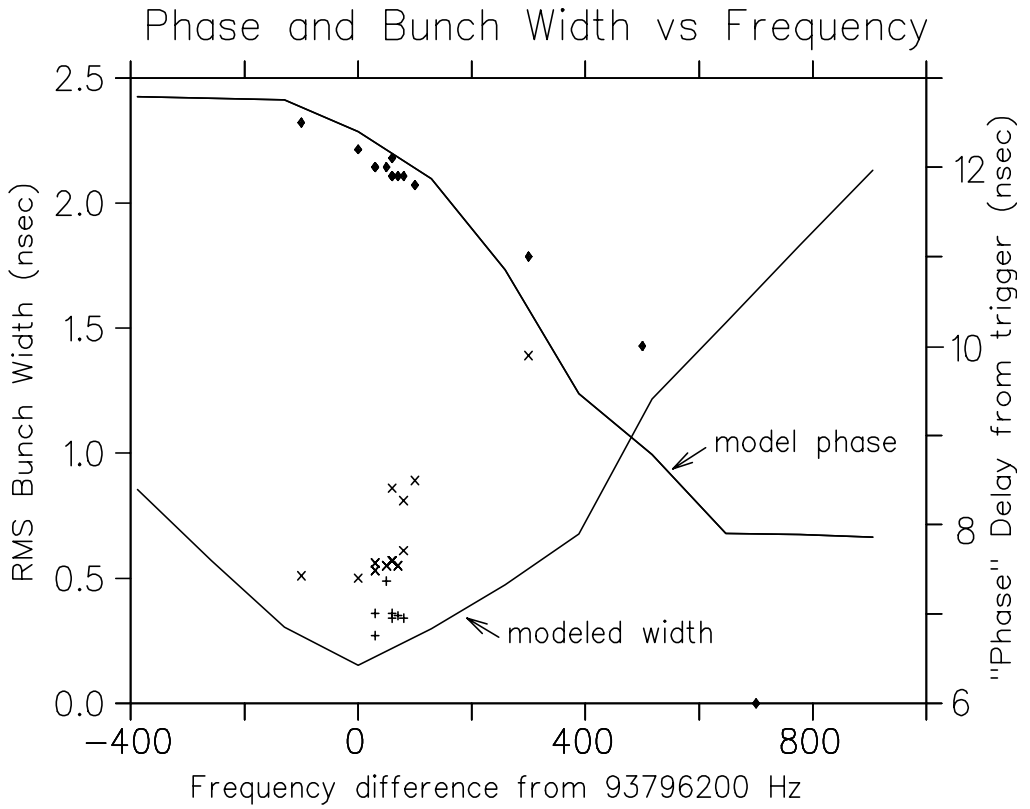

Figure 8: Phase and bunch width vs. frequency difference. The x's are the measured RMS for the entire spill, while the +'s are the measured RMS for the central 15% of the spill. The diamonds are the measured phase delays.

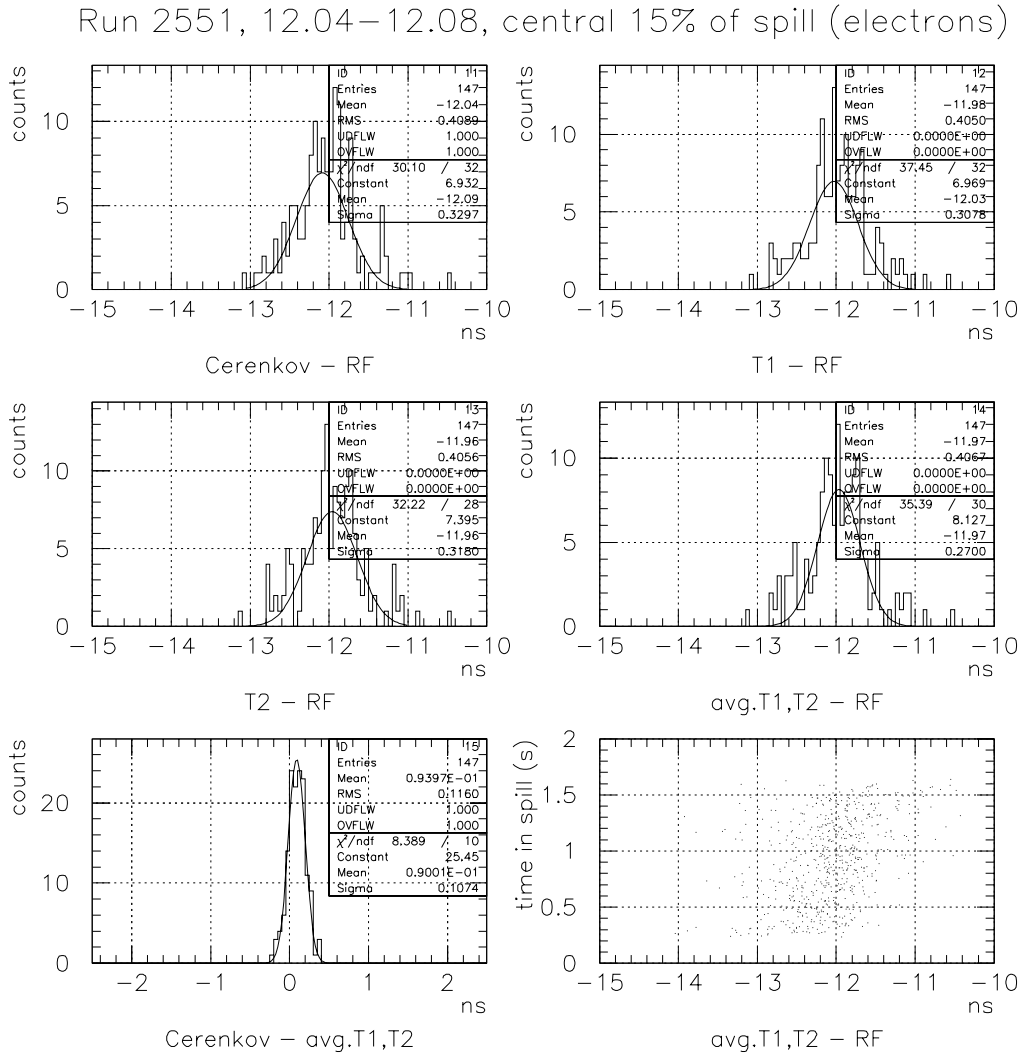

Figure 9: Times measured in scintillation counters (T1 and T2) and in a Čerenkov counter with respect to RF timing. Lower left histogram indicates the system resolution.

is improved, but the present results are already extremely encouraging. For use in the proposed experiment, a new cavity with a lower frequency will be built. Since the minimum RMS bunch width goes as $\sim V^{-\frac{1}{2}}$, we propose to commission a 100 KV, $\sim$ 20 MHz cavity. This is well within the reach of current technology and can be expected to reach a level of $<$ 150 ps which would be more than adequate for our purposes.

3.3 Neutral beam

The spectrum of neutral kaons produced at 45 degrees shown in fig. 10 was obtained using a code based on a fit to CERN charged particle production data [16].[3] A series of precision collimators, followed by scrapers and sweeping magnets will be used to define the asymmetric neutral beam of solid angle 500 μsr (0.004 r vertical and 0.125 r horizontal). The beam contains a K_L flux of 2.5×10^8 per pulse at 10 m from the production target. The neutron spectrum in the beam has been calculated with the ARC code, and with GEANT3 using both the GCALOR [24] and GHEISHA hadronic interaction packages. There is some disagreement among the programs in their prediction of low energy neutrons, but they agree that the n/K ratio at production will be about 2 for neutrons above 1 GeV/c. Most of the potentially troublesome neutrons (those above the pion production threshold, approximately 800 MeV/c) arrive at times later than the kaons of interest.

The neutron halo is expected to be $< 10^{-4}$ of the central beam based on extrapolations of measurements made in AGS E791 which has a similarly narrow aperture as proposed here. One source of the halo can be particles created in the dumping of the primary proton beam. For high energy neutral beams, such as E8 at Fermilab and E791/871 at the AGS, this is an important source of halo because the production angle must be small, and the dump is located near the neutral beam acceptance. For our experiment, due to the large production angle, this source should not be a problem.

A second source of halo is from secondaries scattering from the faces of the neutral beam collimator. This source can be greatly reduced by locating the target upstream of the apex of the collimator acceptance as indicated in fig. 11 so that the particles emitted can't see the collimator faces. For

[3]This code gives results consistent with several recent K_L beams and with other calculations using GEANT3 [23] and ARC [17].

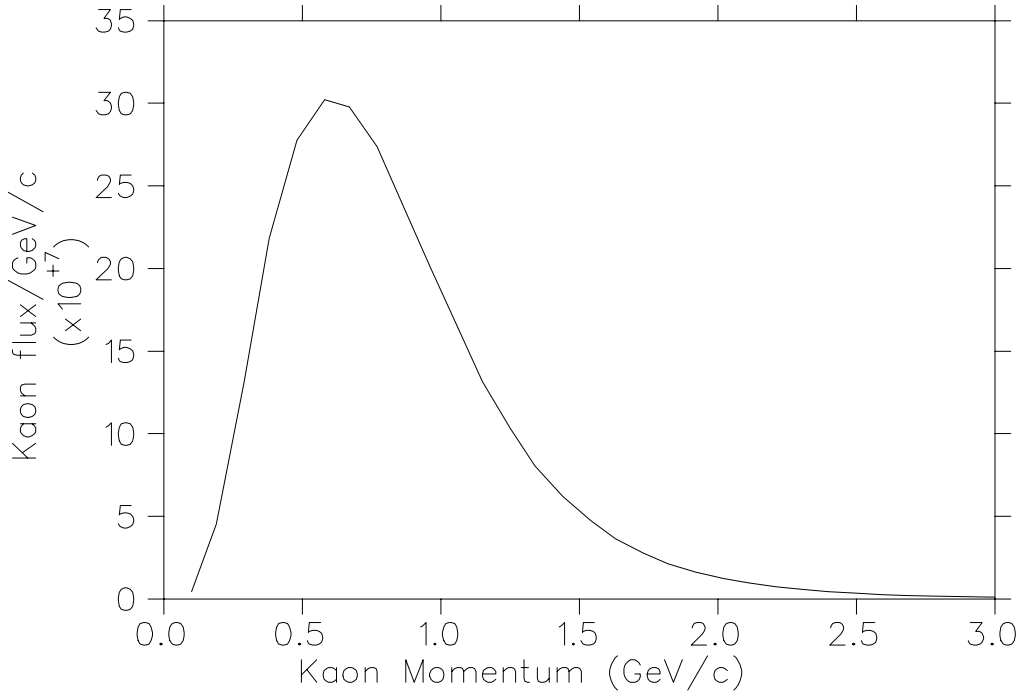

Figure 10: K_L spectrum at 10 m for 5×10^{13} 24 Gev protons striking a 1.2 interaction length target at 45^o into a beam of solid angle 500 μsr. A 5 cm thick gamma filter has been used in the calculations to suppress photons.

example, the 10 cm target (which projects to 7 cm in the horizontal plane) can be placed 50 cm upstream of the apex of the collimator so that particles produced do not see the collimator face. If the collimator aperture begins 5 meters downstream from the apex, the loss in acceptance is 10%. We will locate the vertical collimator apex at the target and begin the vertical collimator aperture close to the target. In this way, secondary scattering in the heat sink above and/or below the target will not see into the neutral beam acceptance.

Another source of halo in neutral beams is the gamma filter. Traditionally it is located downstream after charged particles have been swept away, and in a magnetic field to curl up charged particles produced there. Its purpose is to soften the photon spectrum. Neutrons in the beam will scatter, resulting in halo downstream. We are considering placing the photon converter next to the target, upstream of the collimator apex, but within the triangle formed by the collimator acceptance and target. This must be studied with simulations. We expect that we will be able to soften the photon spectrum without producing particles which contribute to the halo.

The target can be a series of platinum plates, to divide the heating longitudinally, in a water bath. It could be similar to the rotating target used in the current g-2 experiment at the AGS which is designed to accept 60 TP in eight 20 ns bunches. Our experiment will use 50 to 60 TP delivered in a 1.6 s spill. The key point is that the collimator design must eliminate the heat sink as a source of halo.

We plan one sweeping magnet, near the target, with a vertical field of about 20 kG. The coils should be well away from the production plane to reduce radiation effects, with the poles telescoped close to the production plane. A hole in one back leg will allow the primary proton beam to exit. The field and collimator geometry will be optimized by simulating particle production and scattering. The magnet will be similar to a split 18D72.

The beam dump can be located quite far away from the experiment, similar to the g-2 dump arrangement. A second sweeping magnet will be included to remove particles produced in the first defining aperture.

3.4 Neutral beam simulation

To understand the neutral beam line we have initiated a study of the production and transport in the proposed configuration of the neutral kaons,

P_n^{th}(MeV/c)	n/K_L	n/γ
137	27	0.8
445	13	2.3
800	2.6	0.5

Table 3: Calculated neutron to kaon and gamma ratios at 10 m for neutron momentum thresholds P_n^{th}. No gamma filter is used in the calculation.

neutrons and gammas using a Monte Carlo GEANT-CALOR [23, 24] code. Figure 12 shows the momentum spectra of the neutrons at the exit of the last collimator, 10 m downstream of the target for 3.7×10^6 protons on the Pt target. The n/K_L and n/γ ratios at the exit of the last collimator for several neutron momentum cuts are presented in Table 3.

4 Detector

4.1 Choice of design parameters

In an effort to identify the crucial parameters of the proposed experimental apparatus, we have studied the $K^0_{\pi 2}$ background in a number of scenarios. Fig. 13 shows the dependence of the width of the $K^0_{\pi 2}$ background peak (in this case E^*_π the K_L-center-of-mass energy of the π^0 is used) as the resolution in one of the measured quantities is varied from a nominal value shown in Table 2. A notable feature of this study is the importance of the photon angular resolution which is determined primarily by multiple Coulomb scattering effects. The variation of the width of the background peak with energy resolution is another important question dealt with in these studies. It was found that the primary effect of varying the energy resolution in a range from 2 to $4\%/\sqrt{E(GeV)}$ would be to reduce the $K^0_L \to \pi^0\nu\bar{\nu}$ acceptance by about 25% under the constraint that the background rejection power remains constant.

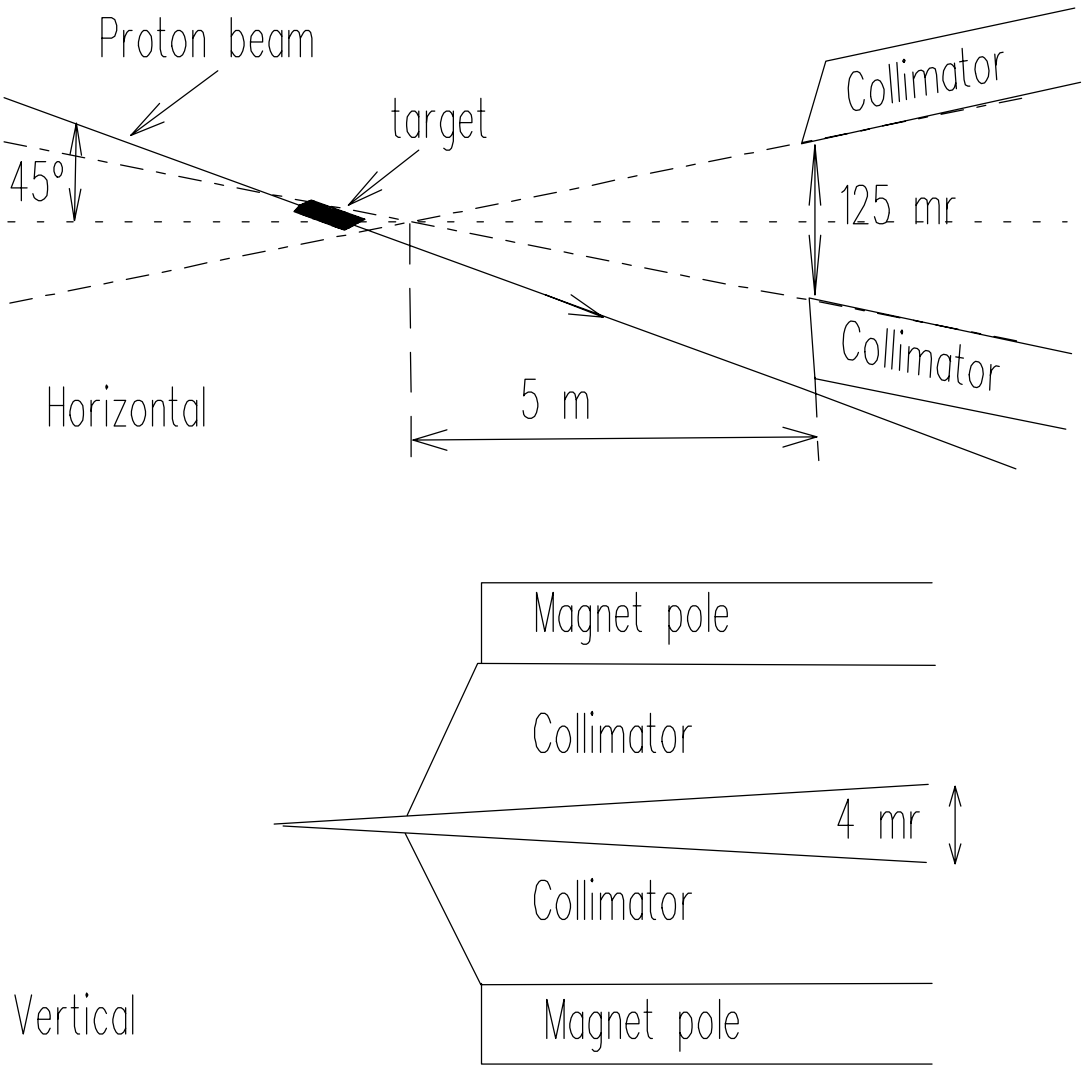

Figure 11: Geometry of the beam line front end (not to scale).

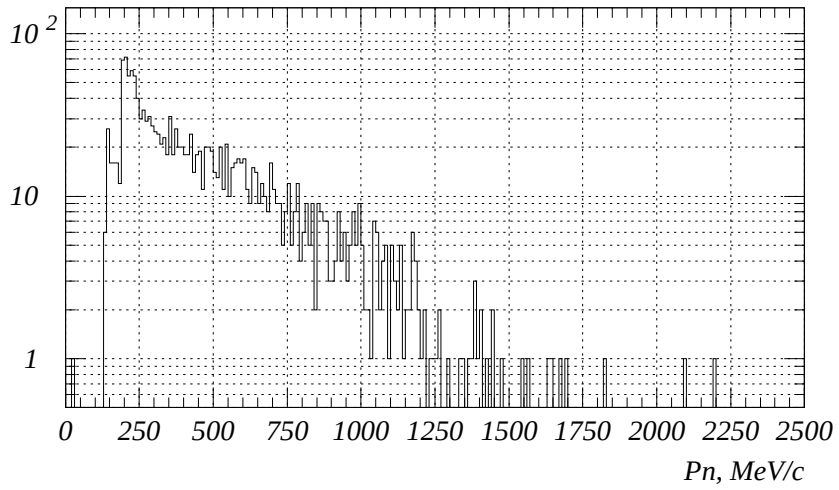

Figure 12: Neutron momentum spectrum at the exit of the last collimator, 10 m from the production target. The low energy cutoff is at E_n=10 MeV.

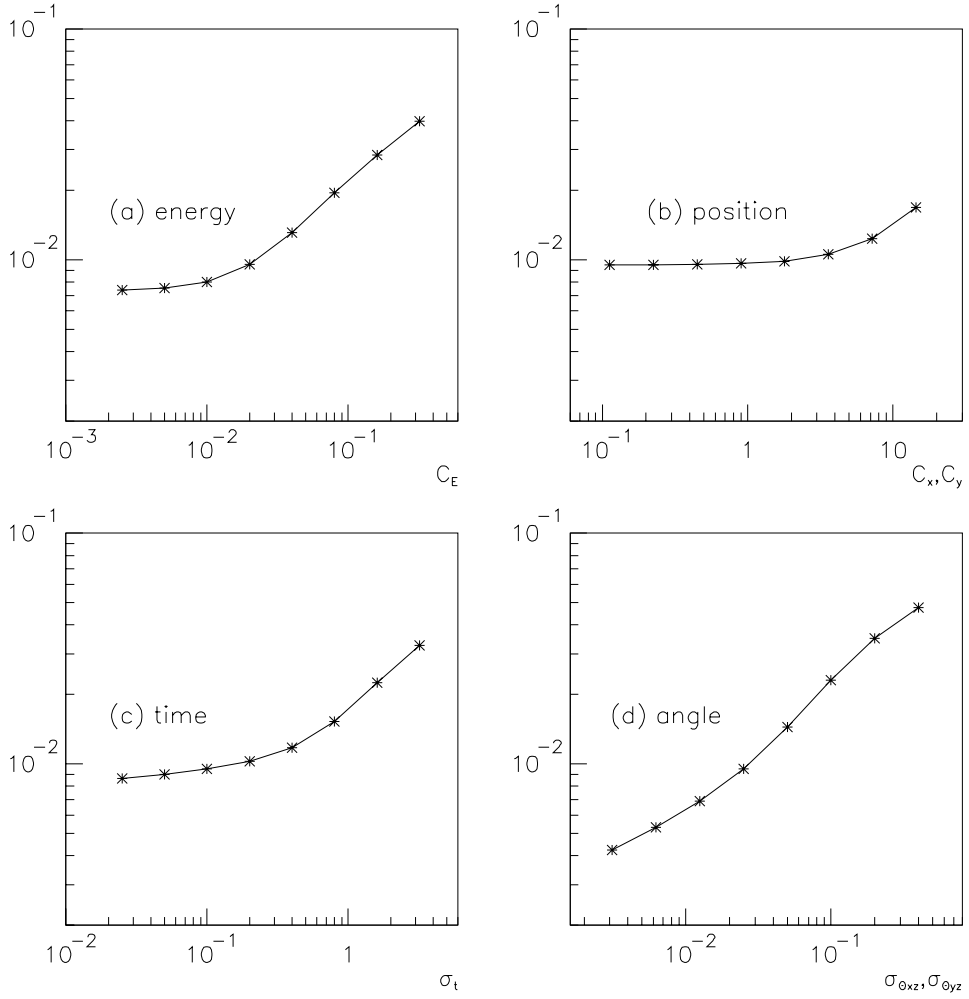

Figure 13: σ's of E^*_π spectra of simulated $K^0_{\pi 2}$ events for different values of smearing parameters. The y-axes are the σ's in GeV. See Table 2 for an explanation of the x-axes. (a) Variation with energy smearing. (b) The same for position. (c) Time. (d) Angle.

4.2 Preradiator

The requirements of the preradiator include a photon angular resolution of approximately 0.02 r, a photon conversion efficiency of about 0.7 (1.5 X_0), a good measurement of the deposited energy and as short as possible linear extent. The principle we will employ is to measure the x and y directions of the first electrons in the shower in a series of thin converter/detector modules. To keep multiple scattering of these electrons at the 0.02 r level each detector module will be $\leq$0.05 X_0. Since our position resolution will be roughly 200 μm, the detector modules must then be separated by about 1 cm.

The primary preradiator arrangement under consideration employs 42 modules illustrated in fig 14. Each layer consists of a 2 mm thick x 16 cm wide scintillator (either scintillator plate or arrays of fibers), a layer of drift chambers or straw tubes with sense wires separated by 10 mm and 5 mm wide cathode strips running perpendicular to the wires, and a 0.035 X_0 thick metal radiator. Mechanical rigidity is given to a module by pleating the metallic radiator, thus avoiding the need for heavy frame structures around the beam region. The thicknesses of scintillators and radiators are similar to that of the calorimeter so that the energy resolution will be largely unaffected by the preradiator.

The position resolution in the direction perpendicular to the wire will be determined from the drift time, within about 150 μm. The left-right ambiguity is solved by extrapolation from the subsequent layers. The position measurement along the wire direction comes from the induced charge on the cathode strips. The cathode position resolution is expected to be $\leq$ 200 μm which is estimated from experience with comparable length cathode strips used in the E787 central drift chamber.[4] The opening angle of an electron-positron pair produced by a 200 MeV photon is of the order of 5 mr but the subsequent transport in the preradiator is rather dominated by multiple scattering and other effects. Since the cathode strip position measurement is determined by the average location of the charges due to an electron-positron pair while the anode hit comes from the closest track to the wire, alternating

[4]The E787 drift chamber obtains about 700 μm resolution from the cathode strips which run at 45 degrees to the wires. In the present case the integration time will be an order of magnitude shorter (about 90 ns instead of up to 800 ns for the larger E787 cells) leading to an improvement in signal to noise, the dominant component in the resolution, of a factor of three.

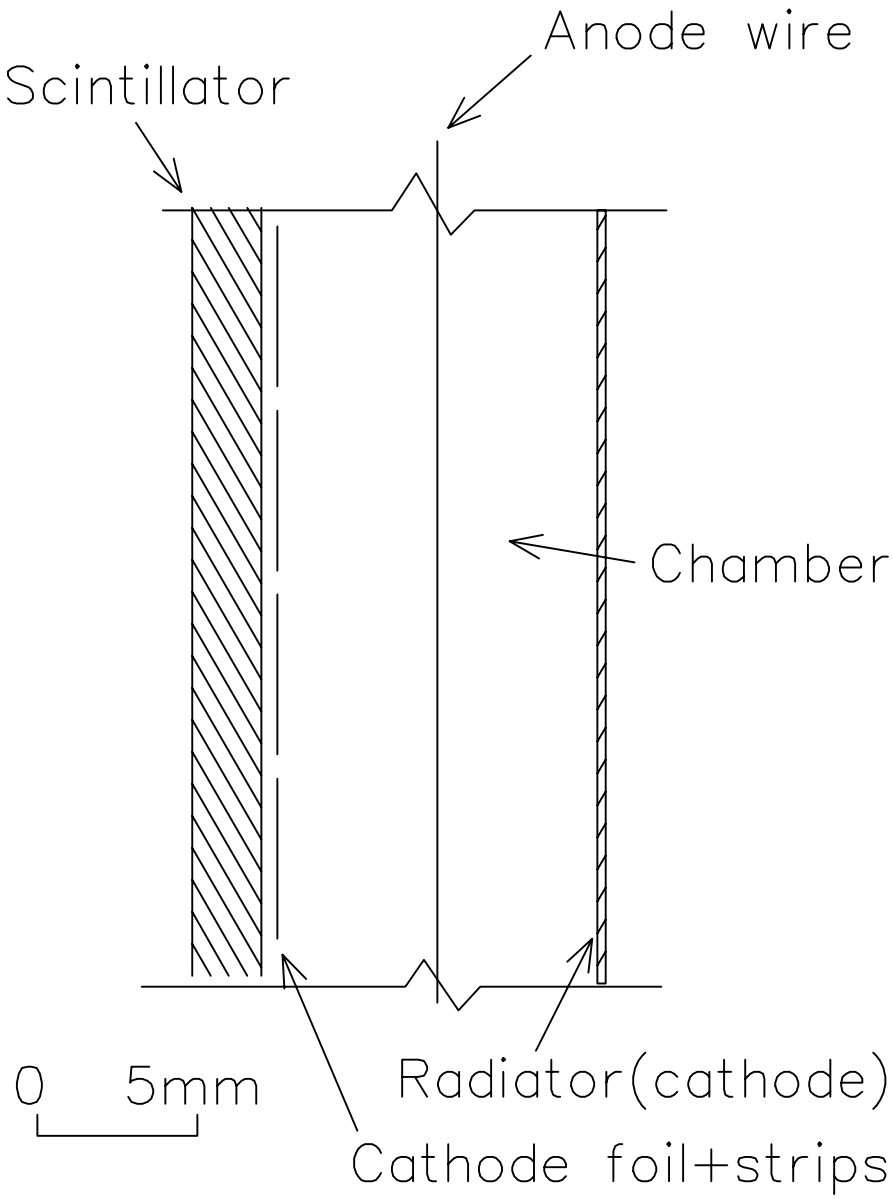

Figure 14: Schematic of a preradiator layer.

the anode and cathode angles in every other layer provides the information needed to determine the photon direction. In order to avoid a possible high rate problem near the beam region, anode wires may be strung at 45^o with respect to the vertical direction. In this case the strips would run at -45^o. This arrangement uniformly distributes the particle rates (due to the beam halo) among the wires and reduces the chance of having two hits on the same wire or strip which causes ambiguity in the hit assignments. The total rate at the entrance of the preradiator is due to charged particles from K_L^0 decays and may be as high as 20 MHz shared by 300 wires. The hottest wire may be counting at 100 KHz.

The total numbers of channels for anodes and cathodes are 25K and 50K, respectively. In order to minimize the cost and take advantage of the potential for pipelining made possible by the bunched beam time structure, digitization will be done on-board at the chambers. The cathodes will employ switched capacitor arrays and multiplexed ADC's and we are considering the use of an on-board 500 MHz clock in phase with the machine microbunch for time digitizing of the anodes.

The number of scintillator channels is about two thousand which may be multiplexed among several layers for readout. The scintillators may be oriented vertically and shifted by a half width for every other layer to reduce ambiguity. In this geometry, the attenuation of the light in the scintillator can be corrected for the energy measurement by using the chamber hit-position.

In addition to the arrangement described above, a scintillation-fiber tracking option is also being considered. In this design, there are 30 layers of sandwiches of three 1 mm thick scintillator-fiber planes (in one plane the fibers run horizontally and in two planes fibers run vertically), three 0.013 X_0 lead sheets and a 1.2 cm gap. The resolution expected for a single layer is 1 mm/$\sqrt{12} \sim 300\mu m$ (which could be improved by a factor of 2 by adding another layer of fibers shifted by a half fiber-width).

The horizontal fibers are 4.3 m long and cross the preradiator from one side to the other, while the vertical fibers are 2 m long and the beam pipe separates upper and lower sections. In order to reduce the number of readout channels to a manageable value for conventional phototubes, the fibers can be grouped by 200 (20 cm wide) with each end of a fiber multiplexed into two different readout channels. One possible multiplexing arrangement for the horizontal fibers is as follows: at one end 20 consecutive fibers (e.g. (1-20), (21-40)...) are viewed by one phototube whereas at the other end,

every twentieth fiber (e.g.(1,21,41...),(2,22,42...)...) is viewed by another phototube. This uniquely determines which of the 200 fibers is hit if there is a single hit. The gain and attenuation can be corrected for each fiber. The chance of having two random hits (other than hits by the same e^+e^- pair) within a group of 200 fibers, assuming a total hit rate of 10^7Hz, a 2 ns time resolution and 20 fiber groups, is $\leq$0.1%. If coincident hits occur there will be a maximum of N^2 possible assignments where N is the number of hits. For the vertical fibers, only one end of a fiber is accessible so two layers of fibers overlapping each other can be treated like the two ends from one fiber for multiplexing purposes. Then, the same type of multiplexing scheme as for the horizontal fibers can be applied. However, in this case each pulse height measurement is independent and attenuation effects will be be corrected by using the position information coming from the coincident horizontal fiber location. The total number of phototubes in the all fiber preradiator would be about 36 K.

4.3 Calorimeter design

In the $K_L^0 \rightarrow \pi^0\nu\bar{\nu}$ experiment configuration, the endcap calorimeter occupies an area of 4 x 4 m^2 behind the preradiator. The optimization study described above and other considerations lead to the following requirements for the calorimeter:

1. Time resolution approximately 60 ps/ $\sqrt{E(GeV)}$
2. Energy resolution 2 - 4%/$\sqrt{E(GeV)}$
3. Granularity 10 cm

In considering the design of the calorimeter we examined through GEANT simulation the consequences on overall energy resolution of placing the 1.5 X_0 active preradiator described above in front of an ideal calorimeter. The result was that preradiator "spoiling" amounted to an added component of approximately 1%/$\sqrt{E(GeV)}$ and therefore has little consequence on the overall photon energy resolution.

A natural choice to satisfy the requirements of the experiment might involve the use of 18 X_0 of pure inorganic crystals such as BaF_2 or CsI with fast light output components. Resolutions of $< 2\%/\sqrt{E(GeV)}$ would

be expected. In this regard, we are exploring the use of a 2.5 m^2 array of pure CsI crystals now being used in a K decay experiment at KEK by the Kyoto group participating in this proposal; these crystals will come available sometime in 1997 and are not presently committed elsewhere. However, it may be possible to avoid the significant expense and time delay associated with producing a new crystal calorimeter to cover the remaining 14 m^2 of the endcap detector by advancing the alternate technology of lead-scintillating fiber calorimetry.

Recently, the KLOE group at DAΦNE has constructed a large lead-scintillator sampling calorimeter [25] consisting of very thin (0.5 mm) lead layers in which are embedded 1 mm diameter scintillating fibers. The lead layers and fibers run perpendicular to the incident photons instead of along the fiber direction (as in previous spaghetti calorimeter designs) leading to superior energy and timing resolutions. In prototype modules the KLOE group achieved energy resolution of $\sigma(E)/E = 4.4\%/\sqrt{E(GeV)}$ and time resolution of $34ps/\sqrt{E(GeV)}$ for photons in the energy range 20 to 300 MeV. Little dependence was observed on incident photon angle and entry position within calorimeter modules. Fig. 15 shows the structure of the calorimeter modules which are read out at both ends of the fibers in 4 x 4 cm^2 cells. The KLOE detector employs a 4.3 m long barrel detector surrounding two 4 m dia. endcaps.

In a sampling calorimeter, the energy resolution is determined primarily by fluctuations in the fraction of the shower energy absorbed in the active layers. A large fraction of the energy of an electromagnetic shower is deposited by low energy (<few MeV) electrons generated by the photo-electric effect or Compton scattering. These processes have high power Z dependence and usually take place in the absorber layers with visible energy deposited only by electrons able to escape into the nearest active material. In a fine sampling calorimeter, the energy resolution can be parameterized in terms of the sampling structure and the amount of energy deposited in the active material:

$$\frac{\sigma}{E} = \frac{5\%}{\sqrt{(E)}}(1-A)\Delta^{0.5(1-A)} \tag{9}$$

where Δ is the energy in MeV lost by a minimum ionizing particle (m.i.p.) in one layer (both active and inactive) and A is the visible fraction of energy.

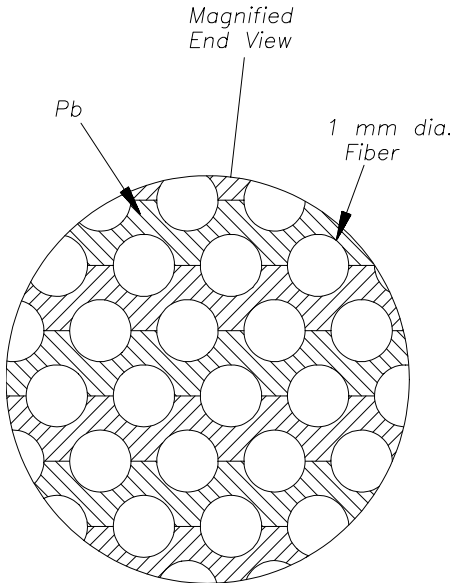

Figure 15: Internal sctucture of the KLOE calorimeter.

As shown in refs. [26] and [27], this expression is valid within about 20% for a wide range of operating calorimeters. For the KLOE calorimeter, the predictions of the formula agree with GEANT simulations[5] and with the measurements cited above (including photo-statistics).

Although the resolutions achieved by the KLOE group are nearly sufficient for the $K_L^0 \to \pi^0\nu\bar{\nu}$ experiment, we would benefit from improvements. We are therefore investigating a similar structure that also uses 1 mm dia. fibers but has the lead layers reduced in thickness by a factor of three, to 0.17 mm. In this configuration, the visible fraction of light increases by a factor of 2, to 0.33, and, thus, a significantly lower energy spectrum of electrons can escape from the inactive medium. The calorimeter density will be about 2.2 g/cm^3 and the Moliere radius will be about 8 cm. For such an arrangement we may anticipate an energy resolution of $< 2.8\%/\sqrt{E(GeV)}$ including a 2.3% contribution to the constant from sampling fluctuations and 1.5% from photo-statistics. We are presently developing a GEANT simulation of this

[5] A specially tuned version of GEANT was used to accommodate properly the important low energy processes.

structure and expect to construct and test a prototype calorimeter module.

4.3.1 Calorimeter construction

The $K_L^0 \to \pi^0\nu\bar{\nu}$ endcap calorimeter will be similar in area to one of the KLOE endcap calorimeters which covered a circular area of diameter 4 m. Although the KLOE endcap modules had 90 degree bends, in our case, all modules will be straight and of uniform size (comparable to the KLOE barrel modules) simplifying manufacture.

The calorimeter modules will be assembled by gluing 1 mm dia. single clad fibers between thin grooved lead plates which have been deformed using techniques developed by the KLOE collaboration. They used foils of 6 m length and 15 cm width which were produced using high precision grooved rollers of hardened steel ground to shape by a sintered diamond tool. The groove thicknesses in the KLOE lead plates were uniform within a few tens of μm and deviated from straight lines by less than 0.1 mm. Optical epoxy manufactured by Bicron was used to attach the fibers to the grooves. The grooves can be made large enough so that the fibers are not squeezed by subsequent layers.

Suitable fibers with peak emission at about 435 nm are made by Bicron (BCF-12), Pol. Hi. Tech. (POLIFI 044-100) and Kuraray (SCSF-81); these fibers typically have rise times of 2.5 ns, attenuation lengths in the neighborhood of 3.5 m and light output 3 to 5 photoelectrons/mm (at 4 cm with a standard photocathode) for a m.i.p. We have contacted the first two of these suppliers to confirm their manufacturing capabilities. In addition, Pol. Hi. Tech. has indicated to us that they are performing tests to evaluate the forming of 0.2 mm lead sheets for calorimeter construction. The fiber pitch we expect to use will be about 1.3 mm resulting in a structure with a fiber:lead:glue volume ratio of 72:21:7. This calorimeter structure will have a radiation length of approximately 3.5 cm (compared to 1.6 cm for the KLOE design) and will be rigid and machinable.

The light collection system developed by the KLOE group will be used. It employs a tapered mixing section and a Winston cone which concentrates the sensitive fiber area onto the phototubes yielding an area reduction factor of 2.7 while maintaining 90% of the light.

The $K_L^0 \to \pi^0\nu\bar{\nu}$ endcap calorimeter will use 2.5×10^6 1 mm dia. fibers of length 4.3 m. This represents roughly half the number of fibers used in

all the KLOE calorimeters. Segmenting the calorimeter into regions of 6 x 6 cm^2 read out by a 2 in. phototube on each end results in approximately 1200 channels required.

4.4 Veto detectors

4.4.1 Barrel detector

Suppression of most backgrounds is provided by a hermetic high efficiency photon detector. Several techniques are being considered for the barrel photon veto detector which will have thickness of 18 X_0. The leading possibility is the KLOE calorimeter design with 0.5 mm lead. It has excellent sampling efficiency and high light output giving excellent timing and energy resolutions as discussed above. The barrel detector for the $K_L^0 \to \pi^0 \nu\bar{\nu}$ experiment will be very similar in size to the KLOE barrel and therefore would also require about 2×10^6 1 mm dia. fibers. The barrel sections here would have 90^o bends at the ends for readout (just like the KLOE endcap modules) so that hermeticity of the photon veto system would be maintained.

We will also mention another alternative we are investigating, layers of $\leq$ 1 mm lead and 5 mm scintillator, which could be simpler and less expensive to manufacture. To read light from the scintillators an embedded wave length shifting fiber (WLS) technique can be used[18]. The WLS fibers are placed in the grooves which run along the 4 m scintillator slabs with spacing of 10-15 mm to get both transverse and longitudinal uniformity in the light yield. The summed output of phototubes reading out both ends of the fibers shows less than a 10% variation over the length of the scintillator in the case of BC408 scintillator with 6 m BCF92 fibers[18]. In this experiment the BC408 (Bicron) and multiclad WLS fiber with dopant Y11 (Kuraray) glued in the grooves with silicon based glue (for example SE777) can be used. The WLS fiber uses K-27, a green-emitting compound, as the dopant. The fiber of 1 mm diameter has an attenuation length of about 4 m. In order to reduce attenuation, the WLS fiber can be spliced to a clear optical fiber with attenuation length of about 10 m[21]. Multiclad fibers provide a factor of 1.4 to 1.8 larger light yield than single clad fibers because of the increase of the numerical aperture due to the lower refractive index of the outermost cladding. The clear fibers have an identical multiclad construction. The light yield obtained for 5 mm thick and 10 mm wide scintillator and 1 mm diameter 4 m length WLS fiber

with both ends readout is 40-50 photoelectrons per m.i.p. with a standard bialkali HAMAMATSU R-580 phototube[19]. For the barrel geometry with long and wide scintillator plates the light yield at the level 20 photoelectrons per visible MeV energy loss in the scintillator is expected. This number is somewhat larger than obtained in the BNL E787 barrel veto. The multiclad fiber can be bent into single-turn loops with radii as small as 1 cm before the light loss reaches 3%. An aging study showed no change in light transmission through small loops of multiclad fibers after an interval of seven months[20]. This allows one to simplify the fiber readout at the both ends of the barrel with little dead space between the preradiator detector and barrel veto.

4.4.2 Upstream and other detectors

In the upstream endcap veto region we are considering a tower configuration consisting of very thin interleaved lead and scintillator plates read out by WLS fibers. If one module has, for example, 0.6 mm thick lead sheets as the absorber material and 1 mm thick scintillator (e.g. Kuraray SCSN-81) with WLS fibers spaced by 4 mm, it will produce about 1300 photoelectrons per GeV deposited energy and give an energy resolution $\sigma/\mathrm{E} = 6\%/\sqrt{E}$ [22]. The radiation length of this module is 1.5 cm and the Moliere radius is 3.5 cm. An important feature of a detector comprised of such modules is the absence of physical boundaries between the modules. This provides a light yield uniformity $< 0.5\%$. For gammas with energies close to a veto threshold of say, 5 MeV, a light yield of about 6 photoelectrons is produced. Reduction of the thickness of the lead plates by factor of 2 would increase the light yield by factor 2.

We are investigating the possibility of having the calorimeter and veto counters (barrel and endcap) read out by phototubes produced in Russia by the company MELS (Moscow). Parameters of FEU115M tubes are given in Table 4.

4.4.3 Charged particle vetoes

Vetoing charged particles is important for suppressing background modes such as K_{e3} and for reducing the trigger rate. To accomplish this function, the first layer in each of the photon detectors and vetoing systems will consist of at least 1 cm thick scintillator. In the downstream beam hole direction

Photocathode diameter	25 mm
Number of stages	12
Quantum efficiency at 490 nm	15%
Gain	6×10^6
Rise time	$\leq$4 ns
Nonlinearity up to 80 mA peak current	$\leq$2%
Nonlinearity up to 200 mA peak current	$\leq$10%
Rate at 3 p.e. threshold	10 Hz

Table 4: Specifications for Russian FEU115M phototubes.

beyond the calorimeter, charged particles will be swept out of the neutral beam with a bending magnet into veto scintillators. We anticipate achieving charged particle veto inefficiencies of $< 10^{-3}$.

4.4.4 Beam Catcher

Since the downstream beam hole represents a potentially serious inefficiency in the photon veto system a "catcher" detector must be included in the experimental arrangement. While the catcher must have a good photon detection efficiency ($O(10^{-3})$), it must also have low sensitivity to hadrons to avoid a high rate of "accidental" veto spoiling.

The catcher is designed to veto decay photons whose trajectories are directly in the beam. Those photons which pass through the beam hole, but leave the beam region further downstream will be vetoed by other counters surrounding the downstream beam pipe (see the experimental layout drawing fig. 4). In order to minimize the number of decay photons that must be vetoed by the catcher, the catcher's solid angle as seen from the decay volume must be as small as practical. To reduce this solid angle and to make maximum use of the primary beam time structure (which forces all residual gammas to arrive simultaneously several ns prior to the earliest kaon decay product, and similarly allows elimination of counts induced by the large number of low energy neutrons), the catcher will be located a relatively long distance (10 to 15 m) downstream from the calorimeter.

To minimize hadron interactions while maximizing photon detection efficiency, it is desirable to employ a detector medium for the catcher that has a small ratio of radiation length to interaction length, X_0/λ_I. Various

Material	X_0 (g/cm^2)	λ_I (g/cm^2)	X_0/λ_I	Density (g/cm^3)
Scintillator	43.8	82.	0.54	1.03
Lucite	40.6	83.6	0.49	~ 1.2
Pb	6.37	194.	0.033	11.35
CsI	8.4	167.	0.05	4.53
Liquid Xe	8.48	169.	0.050	3.52
Pb/Lucite	6.67	99.3	0.067	2.14

Table 5: Potential beam catcher detector materials. The Pb/Lucite ratio used is 1:5 by length.

possibilities are listed in the Table 5.

The most suitable choice is a 10 X_0 Čerenkov counter which is blind to low energy protons and charged pions and responds primarily to π^0s produced in the material of the detector itself. The counter should be highly segmented and directionally sensitive to maximize its sensitivity to high energy photons from the decay region and to suppress interactions caused by low energy particles produced at larger angles. Liquid Xenon presents an interesting possibility which we are investigating. However, we are primarily considering a Pb-Lucite sandwich counter which is economical to construct and employs well known technology.

A lead-lucite detector using 50 layers of 1 mm lead and 5 mm lucite, read out from the top and bottom is a prime candidate.[6] The Čerenkov light from a $\beta = 1$ particle entering perpendicular to the lucite surface is trapped by total reflection and transmitted to photomultiplier tubes. From experience with the E787 beam Čerenkov counter and barrel veto, we expect 1 photo-electron per MeV of incident photon energy. The total internal reflection condition sets a minimum momentum for producing a signal of 1.1, 300, and 2000 MeV/c for electrons, pions and protons, respectively. Because neutron induced charged pions and photons from π^0 decays do not always go along the original beam direction, some angular selection in this counter will further

[6] An extra Be absorber may be added between the lead and lucite to further suppress low energy photons.

suppress background rates. Using the beam particle fluxes given in this proposal, and known neutron scattering and pion production cross sections, we estimate that the instantaneous rate in the catcher during the signal arrival window will be less than 20 MHz. This will result in $< 4\%$ loss with a 2 ns veto timing window. With a horizontal segmentation of 40 the counting rates in individual phototubes would be about 1 MHz. If higher than anticipated beam rates were encountered, pileup problems can be addressed by further segmentation and by locating the catcher further downstream. Although the E787 beam counter has operated without problem for many years in a flux of ~ 1 MHz/cm^2, we are investigating the potential issues of radiation damage for this application.

A Pb-Lucite counter located 15m downstream of the exit of the main detector will have an active volume approximately 12 cm high, by 375 cm perpendicular to the incident beam, by 30 cm along the beam. It would be viewed from the top and bottom by 40 phototubes, uniformly arrayed along the long dimension of the counter, perpendicular to the beam. We expect to perform GEANT simulations and to gain experience with prototype counters in a test beam before a final design is made.

4.5 Vacuum and Mechanical Considerations

The decay volume and the entire beam path for the K^0_Ls (and accompanying neutrons), from the production target to the downstream catcher, must be at high vacuum (10^{-7} torr) in order to suppress background from neutron interactions with the residual gas producing π^0s. The walls of the vacuum containment must be of minimal material in order to minimize photon conversion and also photon production from charged particles, for example, in K_{e3} decay via charge exchange and annihilation. The high-vacuum constraint precludes materials subject to significant out-gassing, either in the vessel itself, or in the form of detector systems within the vacuum volume. A metallic vessel inside the photon detection systems would be suitable if the walls and/or the support structure can be thin enough.

The collimated beam will be narrow in vertical angular spread (4 mr) and wide in horizontal angular spread (125 mr) to give a nominal cross section profile of 4 cm vertical (Y) by 1.5 m horizontal (X) in the detector. A beam box of nominally 20 cm in Y by 1.8 m in X will extend from the target/filter/collimator region to the upstream end of the detector assembly

(10 m). It will be stiffened in the X dimension by external ribs, and will include a high vacuum pumping station. A similar but larger (to follow the expanding beam) box will extend from the downstream end of the detector to the catcher. Elliptical geometry may provide the optimum strength verses minimum mass in these areas.

Within the photon detector/veto array, the general dimensions of the vacuum vessel are constrained by the nominal decay volume length of 3.5 m, and by the extent of neutron beam halo surrounding the nominal beam profile. In the design under study, the main structure of the vessel will be cylindrical, or nearly cylindrical (elliptical) as indicated in fig. 16. The main axis is on the beam axis and the vessel is essentially a variation of the beam sections with the vertical dimension of the ellipse increased, approaching a circular shape. The upstream and downstream ends will be elliptical transitional sections with the vertical dimension varying to match the beam section at one end and the detector section at the other. Wall thickness at all points will be minimized using external ribs and/or undulated (corrugated) shapes. There may be some additional mass in the form of flanges, struts, etc., to support the vacuum vessel in the detector and to support some of the atmospheric pressure load.

The design goal in the direction of the photon preradiator is 5% X_0. Various techniques have been used to produce thin vacuum vessels, in order to reduce eddy current losses in accelerators, or simply to reduce material costs. Ribbed elliptical structures [28] have been developed for DESY II, and corrugated cylinders have been constructed to contain large gravitational wave detectors [29]. These examples can be scaled to our required dimensions using standard engineering formulae [30]. Actual thickness dimensions depend strongly on details of the structure and on acceptable safety allowances. The conventional construction has been in stainless steel. However in order to achieve the thickness goal, other materials will be explored to provide a better strength to mass ratio. A small (10%) gain using other steel alloys is possible where non-magnetic properties are not required. Aluminum or aluminum-titanium alloys can give up to a factor of two reduced radiation lengths and energy loss. Exotic materials such as beryllium and carbon fiber composites can give factors of 3 – 4 over stainless steel. Although beryllium is not practical for large structures, metalized carbon fiber composite and honeycomb sandwich structures [31] are under development. Using a combination of sophisticated structural techniques and materials, wall thickness in

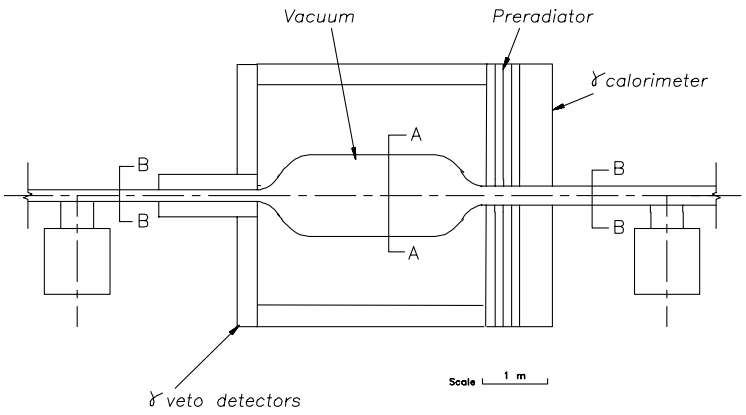

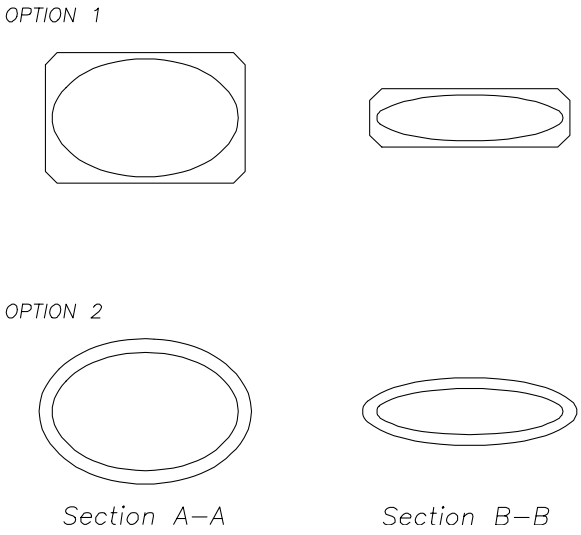

Figure 16: Illustration of vacuum vessel concepts.

the range of a few percent of a radiation length in the critical regions of the detector are expected.

The pumping system required to maintain a base pressure of less than 10^{-7} Torr is straightforward. Since the volume will not be vented often, pump-down speed is not a serious constraint. Provided that the vessel has only metallic surfaces and can be thoroughly cleaned or baked out, out gassing also is not a problem. Either turbo molecular or cryogenic pumping would be suitable, with a modest mechanical pumping system for roughing and backing. Two pumping stations, one each in the upstream and downstream beam boxes will be used.

Other mechanical systems for structural support of the main detector, are expected to be relatively conventional, as there are no exceptional requirements for positional precision. The primary constraints will be to minimize occlusion of detector elements, and to provide for adequate access for assembly and service of detector systems.

4.6 Trigger and data acquisition

4.6.1 Trigger

The trigger will be based on the appearance of two photon clusters in the endcap detector with appropriate spatial and energy correlation and the absence of energy (above O(10 MeV)) detected elsewhere in the detector in prompt coincidence. Signals from phototubes will be acquired using 500 MHz transient digitizers (e.g. GaAs CCD's and flash ADC's as in E787); this technique facilitates achieving maximum timing resolution, reduction of the allowed signal timing window and rejection of coincident pile-up background.

There will be at least two levels in the trigger logic (Level0 and Level1). The Level0 logic is based on conventional NIM or ECL logic. After vetoing on charged particles, the major contribution to the Level0 counting rate comes from the decays $K_L^0 \to \pi^0\pi^0\pi^0$ (21 %) and $K_L^0 \to \pi^0\pi^0$ (0.1 %). Photon veto in the barrel region and a cut on the number of active endcap elements can reduce the Level0 trigger output to less than 10^3 Hz for 10^7 K_L^0 decays/s. At this stage, the two neutral modes above and the decay $K_L^0 \to \gamma\gamma$ are the most significant and contribute to the trigger rate almost equally. The output signal from Level0 will be used to initiate ADC gate and digitizer

Detector	Readout Type	# Channels	Hit data Bytes	# Hits/γ	Data/γ Bytes
Preradiator scint.	TD	2000	30	20	600
Cal & Veto scint.	TD	2500	30	30	900
Tracking anodes	TDC	25000	4	20	80
Tracking cathodes	SCA	50000	12	60	720
All (incl. overhead)					2500

Table 6: A summary of readout data.

trigger signals.

The Level1 trigger can be based on conventional CAMAC or VME modules such as memory look-up units and arithmetic units. Counting the number of shower clusters (instead of the number of hit elements) can be done at this stage. The process may take 100 ns to 1 μs for access to memory look-up units. Transverse momentum conservation, $\Sigma P_i \sin\theta_i = 0$, can be simulated by the equation, $\Sigma T_i \tan\theta_i = 0$ if $\theta \sim 0$ and $P_i \sim T_i$. This means the sum of energy-weighted decay angles (or hit positions) is nearly zero for the decay modes with final states $\pi\pi$ and $\gamma\gamma$ without neutrinos. Combining these two requirements, we expect to be able to reduce the trigger rate to 100 Hz.

4.6.2 Data Acquisition

For the readout system, we will instrument phototubes with short range (512 ns) Transient Digitizers and the tracking system with TDC's on the anodes and SCA (switched capacitor arrays (SCA), 30 MHz, 64 buckets) on the cathodes. All these readout modules will have zero suppression capability and event buffering. A summary of the readout is given in Table 6.

Assuming trigger rates as described in the previous section and the results of preliminary Monte Carlo calculations, we estimate data rates shown in Table 7.

The data will be kept on local front-end crates during the spill and transfered to a host computer in the inter-spill period. The estimated total data

Modes	Trig./spill	# of γ	Data /spill K Bytes
$\pi^0\pi^0\pi^0$	40	6	600
$\pi^0\pi^0$	40	4	400
$\gamma\gamma$	80	2	400
All			1400

Table 7: A summary of data rates.

rate of 1.4M Bytes/spill can be handled easily by one Digital Linear Tape. Such a data acquisition system collects less than 10% of the data presently handled in the E787 experiment.

4.7 Calibration and monitoring

The decay $K_L^0 \to \gamma\gamma$ with a branching ratio 5.7×10^{-4} provides an excellent source for calibration and monitoring in the $K_L^0 \to \pi^0\nu\bar{\nu}$ experiment. The event topology is the same as the $K_L^0 \to \pi^0\nu\bar{\nu}$ and there is no signal in the veto counters. Thus, the K flux, detection efficiencies, false vetoing and reconstruction efficiencies can all be studied and monitored. The event rate is roughly 1 K/pulse so there is no shortage of events to populate the entire detector.

For monitoring the phototube gains we will likely use a Xe flash lamp system as a stable light source.

5 Simulations

An initial GEANT Monte Carlo study of the detector has been done, including simulation of the preradiator arrangement similar to that described above. The simulation included the effects of the varying position of the K_L decay vertex, solid angle acceptance (including the beam hole), and reconstruction efficiency. Fig 17 shows the $\gamma\gamma$ mass distribution for signal events with m_π^0 resolution (RMS) approximately 10 MeV. Figure 18 shows the angular resolution obtained for several photon energy regions. The simulation results were consistent with the nominal values of resolution and acceptance

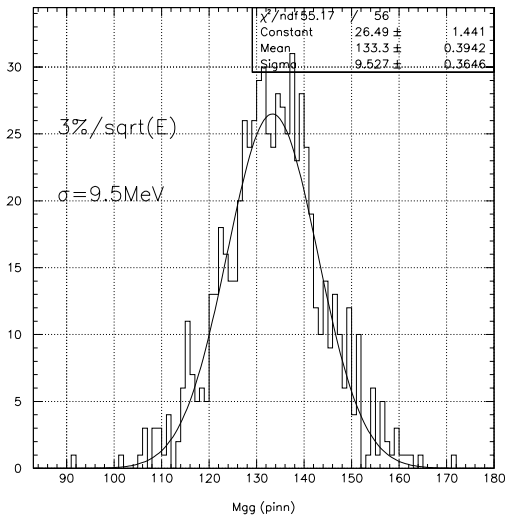

Figure 17: Reconstructed $\gamma\gamma$ mass from the detector simulation.

in Table 2. It is expected that, with further optimization, these resolutions will be somewhat improved.

6 Photon veto

6.1 Detection inefficiency

E787 has achieved π^0 detection inefficiency of 10^{-6} at photon energies of 20-225 MeV using a lead/scintillator detector. The main photon detector consisted of about 1 radiation length of plastic scintillator (range stack) followed by multiple layers of 1 mm thick lead and 5 mm thick scintillator (barrel veto) for a total of about 15 X_0. The inefficiency for the lowest energy photons is $\sim 10^{-2}$ and appears to be mainly limited by sampling fluctuation. The inefficiency for higher energy photons is $\sim 10^{-4}$ and appears to be limited by sampling fluctuations, shower escape and photonuclear reactions which may be contributing at comparable levels. Although the E787 group has attempted to study the origin of the residual inefficiency through measurements and simulations, considerable uncertainty remains. Thus, as-

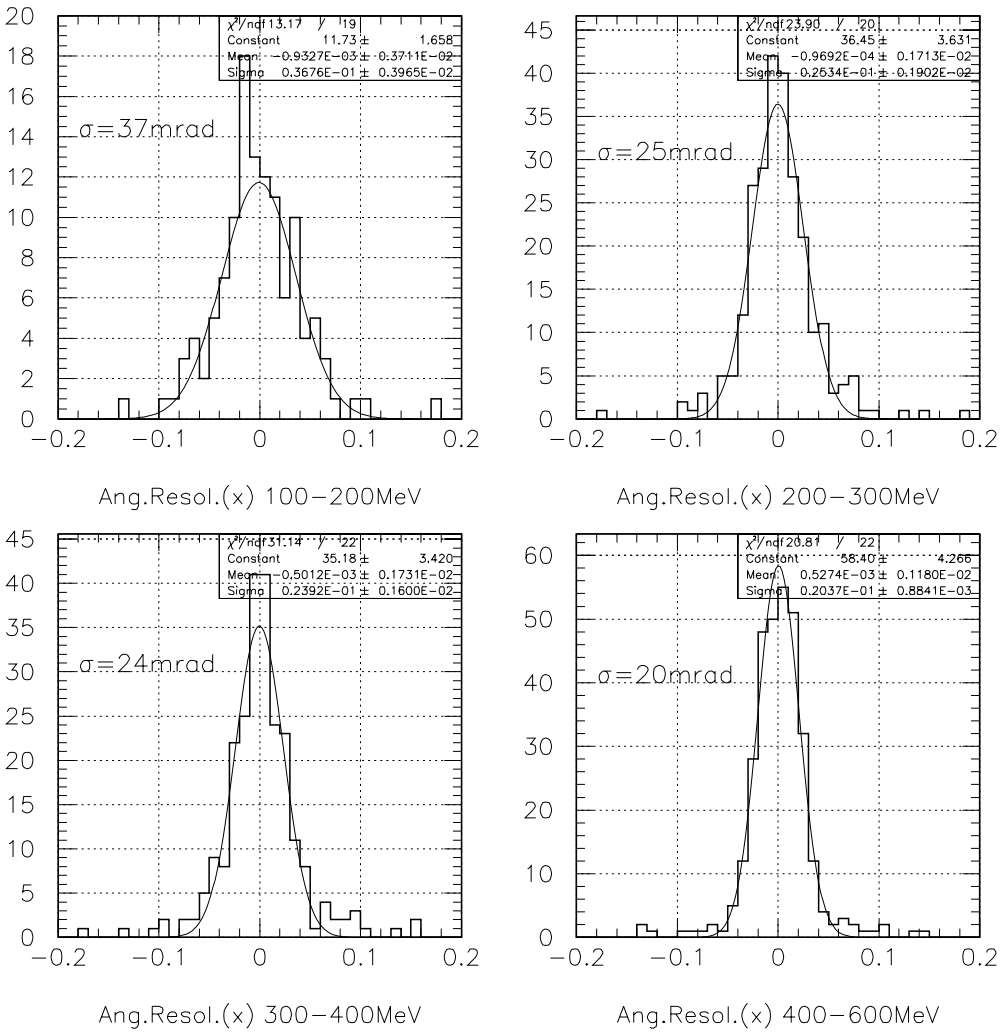

Figure 18: Preradiator angular resolution from the detector simulation. Results for four photon energy regions are shown. The center of gravity of the pair was used in the position determination.

suring the achievement of substantially higher photon detection efficiencies, for instance, at higher photon energies than the existing measurements, may be extremely difficult to establish reliably without actually performing the relevant measurements. The uncertainties are even larger for the region below 20 MeV photon energy which will be preferentially populated by $K^0_{\pi 2}$ background events involving higher energy π^0's than observed in E787. It is for these reasons that, although advancements in detection efficiency may be possible to achieve, we will only rely on small extrapolations from the E787 measurements in predicting the level of π^0 inefficiency.

The goal in the $K^0_L \to \pi^0\nu\bar{\nu}$ experiment is to have π^0 detection inefficiency approaching 10^{-8}. This may be feasible since both photons are generally in the higher energy range of the E787 measurements where single photon detection inefficiencies of 10^{-4} have been measured. Since we also have kinematic handles available, we can suppress those kinematic configurations of $K^0_{\pi 2}$ events with low energy missing photons and reasonably expect to achieve the goal as discussed below.

Small improvements in the photon detection inefficiency for lower energy photons may be possible until the photonuclear limit is reached by using a fully active calorimeter or a finer sampling calorimeter as discussed above. The photon detection efficiency of higher energy photons may also be improved by a small factor until the photonuclear limit is approached by implementing more radiation lengths to block remaining shower escape. In the $K^0_L \to \pi^0\nu\bar{\nu}$ experiment described here, we will increase the thickness to 18 X_0.

6.2 Kinematics for suppressing low energy photons

Because the momentum of K_L is tagged, we can obtain the energy of the missing photons in $K^0_{\pi 2}$ events by subtracting the measured energies of the two observed photons from the K_L energy. Requiring significant total missing energy (i.e. $(E(K_L) - E_{\gamma 1} - E_{\gamma 2})$ as is generally the case for $K^0_L \to \pi^0\nu\bar{\nu}$ events suppresses most potential background events that contain lower energy missing photons (where the inefficiency is greatest). However, in unusual cases when one of the missing photons has very high energy and one has very low energy an additional cut on missing mass (i.e. $\sqrt{(E(K_L) - E_{\gamma 1} - E_{\gamma 2})^2 - (\mathbf{P}(K_L) - \mathbf{P}_{\gamma 1} - \mathbf{P}_{\gamma 2})^2}$) is effective. Because the

missing mass in $K^0_{\pi 2}$ events is proportional to $\sqrt{E_{miss1} * E_{miss2}}$, where E_{miss} is the energy of a missing photon, the missing mass also becomes small for the asymmetric energy sharing case. Figure 19 shows the missing mass vs. missing energy distribution of photons for $K^0_{\pi 2}$ and $K^0_L \to \pi^0 \nu \bar{\nu}$ events. After removing the low missing mass and low missing energy region, we can suppress the low energy photons to achieve 10^{-8} detection inefficiency for the two missing photons in $K^0_{\pi 2}$ events.

6.3 Photon loss through holes and shower escape

The largest aperture in our detector is the downstream beam hole which is covered by the "Catcher". The contribution of the beam hole is estimated to be less than 10% of the overall inefficiency assuming that the photon detection inefficiency of the Catcher is a factor of 10 worse than in the other sections of the detector.

Photons can also hide in the showers of other detected photons. These overlapping photons can occur a few % of the time in $K^0_{\pi 2}$ events when the distance between two photons at the calorimeter is less than 50 cm (about 6 Moliere radii) and less than 1% of the time when the separation is less than 20 cm. When the distance between two photons is 20 cm to 50 cm, one can identify the overlapping photons by comparing the shower center of gravity in the calorimeter which has a position resolution $\sigma \sim 3$ cm with the expected position obtained by extrapolating the preradiator track; assuming an inefficiency of 10^{-3} for the center of gravity method and including the probability of the conversion of the extra photon in the preradiator, the photon veto inefficiency due to overlap is $\sim 10^{-5}$. When the separation is less than 20 cm and the overlapping photons merge, the invariant mass of the photons always becomes much larger than the π^0 mass and the missing energy and mass are small. The inefficiency of this invariant mass cut is limited by the photonuclear reaction probability (a few times 10^{-3}) of the overlapped photon. Again, taking into account the photon non-conversion probability, the photon detection inefficiency due to overlap in the region of separation < 20 cm is also estimated to be $\sim 10^{-5}$.

Due to the relatively large Moliere radius of our calorimeter/preradiator system, some signal events can fail the overlapping cut by sending a "splash" of shower energy outside the single photon acceptance region. A GEANT Monte Carlo simulation was done by injecting 200 MeV photons into the

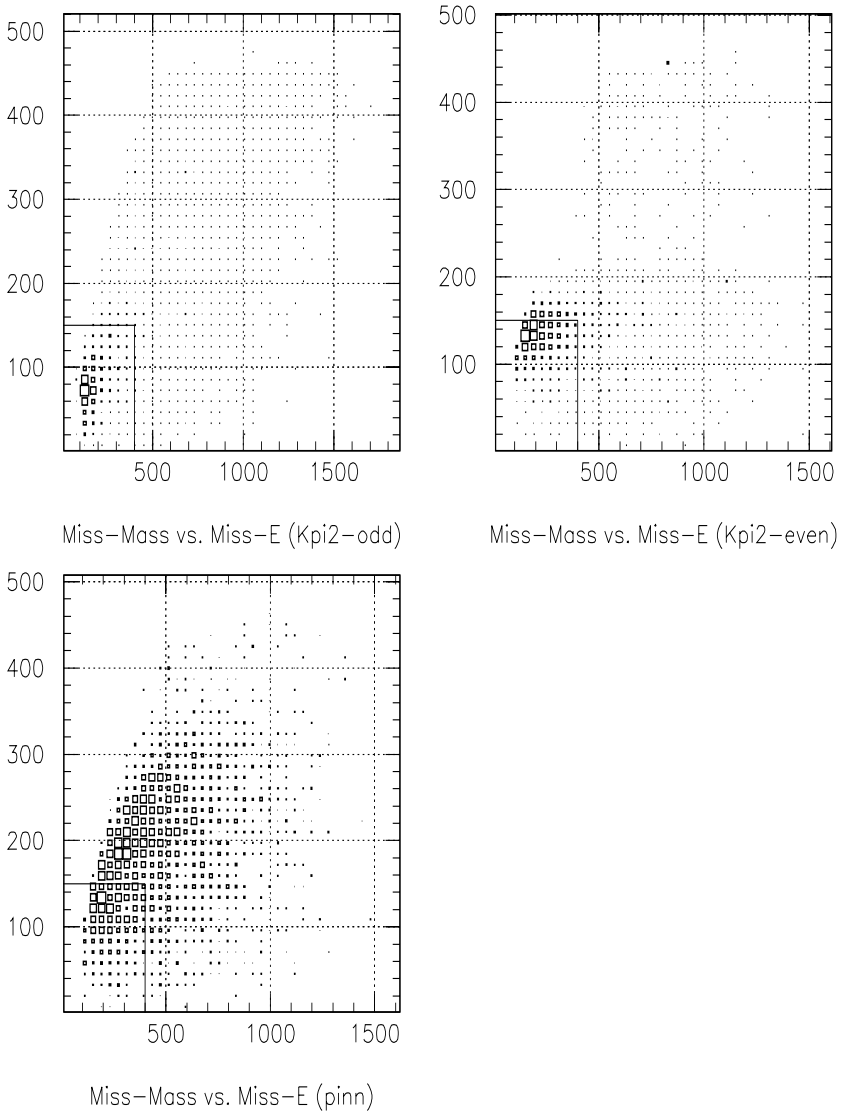

Figure 19: Missing mass vs. missing energy distribution of photons for $K^0_{\pi 2}$ odd, $K^0_{\pi 2}$ even and $K^0_L \to \pi^0 \nu \bar{\nu}$ events.

Requirement	
Solid angle	0.36
$m_{\gamma\gamma} = m_\pi$	0.72
E^*_π	0.38
Photon energy cuts	0.35
Gamma conversion and reconstruction	0.45
Acceptance	0.016

Table 8: Acceptance for $K^0_L \to \pi^0\nu\bar{\nu}$.

preradiator/calorimeter system. Only 2% of the events gave more than 50 MeV outside of the 20 cm radius from the shower center and 1.5% of the events show more than 10 MeV outside the 50 cm radius. The acceptance loss due to this mechanism is estimated to be a few percent.

7 Sensitivity estimate

Table 8 gives factors leading to the estimated acceptance of approximately 1.6%. It includes the solid angle, photon conversion and reconstruction factors and phase space (E^*_π) acceptance in addition to cuts on missing energy and mass and on photon energy sharing. The inefficiency due accidental spoiling of good events is estimated to be < 10 % for a threshold of a few MeV and a timing window of 2 ns. The expected number of $K^0_L \to \pi^0\nu\bar{\nu}$ events to be accumulated for 8000 hours of beam at 5×10^{13} protons/spill is 70. The signal yield is calculated as follows:

$$\begin{aligned} N_K &= (1.9 \times 10^7 \ K_L \text{ decays/pulse}) \cdot (8 \times 10^6 \text{ pulses}) \\ &= 1.5 \times 10^{14} \ K_L \text{ decays} \\ N_{\pi\nu\bar{\nu}} &= N_K \cdot \epsilon \cdot \mathrm{B} \\ &= (1.5 \times 10^{14}) \cdot (0.016) \cdot (3 \times 10^{-11}) \\ &= 73 \text{ events} \end{aligned}$$

and B$= 3 \times 10^{-11}$ is the SM central value for the branching ratio. The single event sensitivity of the experiment would be approximately 4×10^{-13} if not limited by background.

8 Background estimates

8.1 Background rejection

Potential sources of background include $K_L \to \pi^0\pi^0$ events where two of the four photons are missed (the odd and even-pairing cases), neutron production of π^0's, other K_L decays like K_{e3} and $K_L \to \gamma\gamma$ and $\Lambda \to n\pi^0$ decays. Suppression of most backgrounds is accomplished by the hermetic high efficiency photon detector along with kinematic constraints. Our expectations for the efficiency of the photon veto detectors are based on experience with similar detectors in BNL-E787 as discussed above.

The energy and direction measurements of photons by the preradiator/calorimeter arrangement described above along with momentum tagging of the K_L by time-of-flight provide powerful kinematic constraints, such as the mass of the two photons ($m_{\gamma\gamma}$) and the center of mass energy of the π^0 ($E^*_{\pi^0}$). Vertex constraints from photon tracking also help in rejecting accidentals and rejecting particles produced near the surface of the detector by the beam halo. Tight vertical collimation of the beam reduces the beam halos and provides an extra vertex constraint. The 4π coverage of the photon veto ($\overline{\gamma}$) and charged particle veto ($\overline{charge}$) are effective in suppressing other K_L decays. The entire decay volume will be evacuated to suppress production of particles in the decay region.

A summary of the background estimates is given in Table 9. The signal

Process	Modes	Main source	Events
$K_L^0 \to \pi^0\nu\bar{\nu}$			70
K_L decays ($\bar{\gamma}$)	$\pi^0\pi^0$,$\pi^0\pi^0\pi^0$,$\pi^0\gamma\gamma$	$\pi^0\pi^0$	7
$K_L \to \gamma\gamma$	$\gamma\gamma$	$\gamma\gamma$	0.04
K_L decays ($\overline{charge}$)	$\pi^\pm e^\mp\nu$,$\pi^\pm\mu^\mp\nu$,$\pi^+\pi^-$	$\pi^- e^+\nu$	0.01
K_L decays ($\bar{\gamma}, \overline{charge}$)	$\pi^+\pi^-\pi^0$,$\pi^\pm l^\mp\nu\gamma$, $\pi^\pm l^\mp\nu\pi^0$,$\pi^+\pi^-\gamma$	$\pi^+\pi^-\pi^0$	0.003
Other particle decays	$\Lambda \to \pi^0 n, K^- \to \pi^-\pi^0, \Sigma^+ \to \pi^0 p$	$\Lambda \to \pi^0 n$	0.03
Interactions	n, K_L, γ	$n \to \pi^0$	0.5
Accidentals	n, K_L, γ	n, K_L, γ	0.3

Table 9: Estimated event levels for signal and background.

Requirement	$\pi^0\pi^0$ odd	$\pi^0\pi^0$ even
γ combinations	4	2
Solid angle	0.34	0.37
$m_{\gamma\gamma} = m_\pi$	0.08	0.74
E^*_π	0.76	0.008
Photon veto	1.3×10^{-8}	4.2×10^{-8}
Photon energy cuts	0.07	0.17
BR	9×10^{-4}	9×10^{-4}
Photon conversion and reconstruction	0.45	0.45
Acceptance	3.5×10^{-14}	1.6×10^{-14}

Table 10: Acceptance for $K^0_{\pi 2}$ backgrounds.

is estimated to exceed the background by an order of magnitude with the backgrounds dominated by $K^0_{\pi 2}$. We expect that the actual background levels will be determined reliably from the data. In the following we address the most important potential background sources highlighted in the table.

8.2 $K_L \to \pi^0\pi^0$

The dominant background for $K^0_L \to \pi^0\nu\bar{\nu}$ is the CP violating decay $K_L \to \pi^0\pi^0$ ($K_{\pi 2}$), whose branching ratio is 9×10^{-4}. By tagging the K_L momentum as well as determining the energy and direction of γ's, one can reconstruct the kinematics. In the case of even pairing where one π^0 is missing, a kinematic cut on the monochromatic center of mass energy of the π^0 ($E^*_{\pi^0}$) is effective. In the case of odd paring where one photon from each π^0 is missed, the π^0 mass requirement ($m_{\gamma\gamma}$) is effective. Additional photon energy cuts, such as $E^*_{\pi^0}$ vs. $E(K_L) - E^*_{\gamma 1} - E^*_{\gamma 2}$, are also very effective in further suppressing $K^0_{\pi 2}$ backgrounds.

Table 10 gives the estimated acceptance factors for the $K^0_{\pi 2}$ backgrounds. Including all combinations of 2 missing photons out of the 4 photons from $K^0_{\pi 2}$, we expect 5 events from the odd pairing source and 2 events from the even pairing source. These background levels would be further reduced if the photon detection efficiency achieved is better than the conservative assumptions used here and if more detailed study of the kinematical tests proves effective.

8.3 $K_L \to \gamma\gamma$

$K_L \to \gamma\gamma$ is very tightly constrained kinematically. For example, by knowing the direction of one photon, one could know the energies of both photons and the direction of the other photon. Cutting on the monochromatic photon energies in CM system (E^*_γ), using an invariant mass cut on 2 photons($m_{\gamma\gamma}$), and the CM energy of the 2 photons ($E^*_{\pi^0}$) brings this process under control. We expect 0.04 events from this background source.

8.4 $K_L \to \pi^- e^+ \nu$

When the π^- and e^+ react via charge exchange $\pi^- p \to \pi^0 n$ and annihilation $e^+e^- \to \gamma\gamma$ before they are detected, two photon clusters, each of which is made of 2 photons, remain. Inagaki et al.[32] found charged particle veto inefficiencies to be 3.2×10^{-4} for e^+ and 6×10^{-4} for π^- with a veto threshold of 1 MeV.

In our present design, there are two extra kinematic handles on this background: the two photon mass ($m_{\gamma\gamma}$), which tends to be much larger than m_{π^0} and the center of mass energy of the 2 photons ($E^*_{\pi^0}$) which tends to be at the end point of the phase space. Due to the use of a low energy beam, the photons from $\pi^- p \to n\pi^0$ can be identified as two photon clusters, which provides the extra rejection power needed to suppress this mode. The $K_L \to \pi^- e^+ \nu$ background is estimated to be 0.01 events limited by cases where the secondary photons undergo photonuclear reactions.

8.5 $\Lambda \to \pi^0 n$

Because of the large angle of the neutral beam used here, the cross section for producing Λs is low and they decay completely before reaching the decay volume. Backgrounds could arise from Λ's produced by halo neutrons and K_L's. Again, the production cross section of Λs by the beam halo is low because the beam is soft and it is hard for Λs to reach the fiducial decay volume from the interaction point. Good collimation of the beam as well as a vertex cut to eliminate events produced near the surface of the last collimator suppress this background to a negligible level of 0.2 events.

8.6 $nA \to \pi^0 A$

Neutrons interacting with the residual gas in the decay volume can produce single π^0s without any other easily detectable activity. This background is primarily suppressed by having an excellent vacuum (10^{-7} torr) and by the reduced number of neutrons above the π^0 production threshold (800MeV/c) at the 45 degree production angle. The micro-structure of the beam provides further suppression of the neutrons: Figure 20 shows the arrival time of K_L's and neutrons with respect to photons at 10m from the production target. Neutrons with momenta between 1 and 2.4 GeV/c fall into our arrival time of interest (i.e. K_L with momenta between 0.5 and 1.3 GeV/c). Within this time window, the neutron to K_L ratio is improved by a factor of 5. Despite the fact that a low energy beam is used here, the effective n/K_L ratio is as good as or better than in higher energy experiments. This background is further suppressed by the kinematic cuts used for $K^0_{\pi 2}$ because it involves a large unphysical kinematical phase space due to the missassignment of an incoming neutron as a K_L. We expect 0.5 events from this background source.

8.7 Accidentals

Accidental backgrounds are caused by beam halo neutrons, photons and K_L's which are scattered from the last collimator and get into the detector. Multiple stages of collimation of the narrow vertical beam should provide good collimation. From the experience of BNL E791, we would expect to bring the neutrons, kaons and gammas scattered into the detector down to 100 KHz, 100 KHz, and 10 KHz, respectively. Requiring the converted track in the preradiator further suppresses neutrons and K_Ls because they show different track characteristics from photon conversions in the preradiator. Finally, photon tracking allows us to reject those photons coming from the upstream collimators. Assuming the signal event coincidence timing window of 1 ns, the rate of the accidental background is estimated to be 0.3 events.

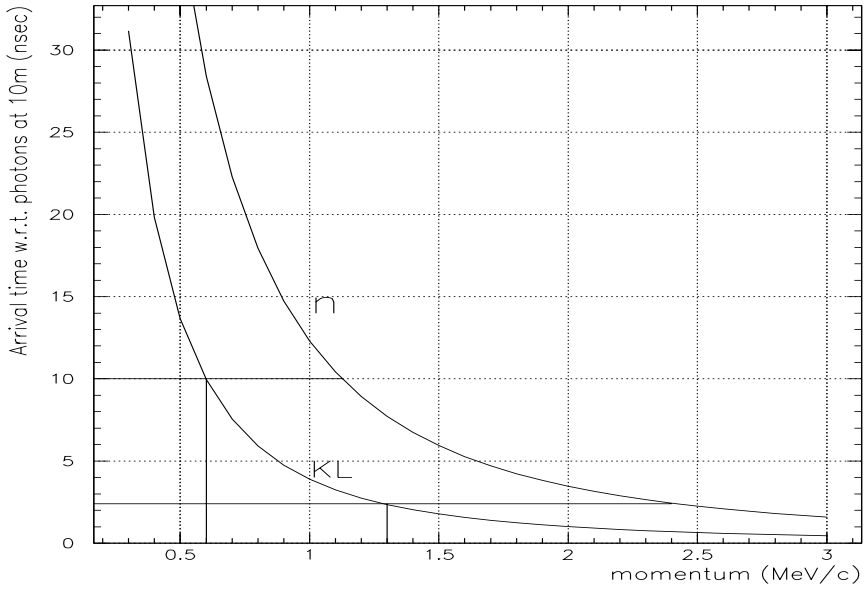

Figure 20: Arrival time of K_L's and neutrons with respect to photons at 10m downstream from the production target.

9 Preliminary measurements and prototyping plans

There are a number of issues that need to be pursued at the AGS:

1. Further microbunching studies. We will continue the series of microbunching studies using the 93 MHz dilution cavity. The beam, beam instrumentation, data acquisition system, and feedback systems can all be further improved. We need data with which to refine the simulations that would enable the final system to be used in the experiment to be designed. When the 20 MHz cavity becomes available, studies using it in concert with the 93 MHz cavity are needed so that the narrowest possible bunches can be achieved. It would be very desirable to get operational experience with the final system before the experiment runs, so that the most efficient possible use of beam time can be made.

2. Measurements of neutral particle production at large angles. Since there is some uncertainty in the large angle neutron production, an early measurement would be very desirable. At the same time we would confirm the predictions of the gamma rates and of the K_L yields. We would welcome a proposal from the AGS on where such a test could most conveniently be carried out.

3. Test beam time is required to test detector prototypes. It would also be desirable to set up a simple tagged photon beam using the electrons in a test beam. Such a facility is needed for testing the angular resolution of the preradiator for photons. It is possible that some of this work can be done at other sites (*e.g.* at the tagged photon beams at LEGS or Tokyo/INS), but it would be very convenient to be able to make such tests at the AGS.

Detector prototype tests will also be necessary: small prototypes of the electromagnetic calorimeter will be made and tested for energy, position, and timing resolution, linearity of response, and other characteristics. Preradiator prototypes planned include single chamber prototypes (to test position resolution, collection time, pulse shape, *etc.*), stacked chamber prototypes (to test angular resolution), single active converter layers (to test fiber light output, uniformity, and mechanical issues) and full preradiator prototypes

Item	Cost(K$)
Calorimeter	3140
Preradiator	3195
Catcher	250
Trigger, DAQ and Digitizers	1625
Vetoes	2913
Vacuum and mechanical	350
Subtotal	11473
Contingency (30%)	3442
Total	14914

Table 11: Estimated costs of the detector itemized in Appendix A.

backed up by calorimeter modules to test overall system performance. Other likely prototypes include the beam catcher, veto counters (barrel, upstream) and electronics such as wave form digitizers, chamber amplifiers and trigger modules.

10 Cost Estimates and schedule

The estimated cost for the detector system is $15M including 30% contingency as indicated in Table 11. The basis for these preliminary estimates is given in Appendix A. It is anticipated that a considerable amount of existing equipment can be used to reduce the overall cost. Although not yet detailed the cost of major items such as the calorimeter are based directly on the actual expenditures on the KLOE calorimeter which was dominated by the scintillation fibers. For the veto calorimeter systems we have also used the KLOE costs which may be more than a factor of two higher than the alternate technologies involving lead-scintillator plates which we are considering. The cost estimate for the vacuum system was made based on conventional stainless steel fabrication and on the pumping requirements indicated above.

We would expect that following a period of minimal R&D outlined above we could initiate production of the fibers and construction of the calorimeter modules late in 1997. Production, assembly and testing would encompass a two year period; much of this may be carried out by industry under group

supervision. Design and construction of the neutral beam line could be completed in one year after which studies of neutron halo would commence. The experiment could be ready for engineering running in 1999 given early approval and funding.

11 Conclusion

A detector system has been presented to measure the rare decay $K_L^0 \to \pi^0 \nu \bar{\nu}$. It is designed to allow definitive observation of a large sample of events with a signal that exceeds backgrounds by an order of magnitude. Special features of the AGS allow provision of an intense pulsed beam of neutral kaons suitable for time-of-flight measurements. Significant redundancies and contingency factors are built into the technique. The standard model origin of CP violation will be confirmed and the complex phase parameter η determined to a precision of $\leq 15\%$ or the absence of $K_L^0 \to \pi^0 \nu \bar{\nu}$ can be established at a level not consistent with the standard model.

Acknowledgments

We would like to thank G. Buchalla and his colleagues for their contributions to the theory section and Gerry Bunce for his work on the neutral beam.

12 Appendix A. Cost Estimates

Preliminary cost estimates for the various components of the experiment are shown Tables 12, 13, 14, 15, 16 and 17. Since we are continuing to optimize the design in several areas, we intend these estimates to be used as a guide to the cost of the experiment. We are investigating several approaches which may lead to lower estimates than those shown.

References

[1] L. Littenberg, *Phys. Rev.* **D39**, 3322 (1989).

Item	Unit Cost	# Units($)	Cost(K$)
Chambers	2000	90	180
Electronics	35	75000	2625
Gas system			25
H.V. system			75
Photubes and bases	90	1000	90
H.V. and cables	100	1000	100
Electronics	100	1000	100
Preradiator Subtotal			3195

Table 12: Estimated costs of the preradiator.

Item	Unit Cost($)	# Units	Cost(K$)
Fibers(4.3m)	1.08	2.5×10^6	2700
Lead(kg)	2.25	18000	42
Photubes and bases	90	1200	108
H.V. and cables	100	1200	120
Electronics	100	1200	120
Mechanical Assembly	50		50
Calorimeter Subtotal			3140

Table 13: Estimated costs of the endcap calorimeter (including the preradiator fibers).

Item	Unit Cost($)	# Units	Cost(K$)
Fibers(4.3m)	1.08	2.4×10^6	2592
Lead(kg)	2.25	54000	126
Photubes and bases	90	500	45
H.V. and cables	100	500	50
Electronics	100	500	50
Mechanical Assembly			50
Veto Subtotal			2913

Table 14: Estimated costs of the veto detectors assuming the KLOE calorimeter design.

Item	Unit Cost	# Units($)	Cost(K$)
Vacuum vessels and pumping system			300
Other mechanical structures			50
Mechanical Subtotal			350

Table 15: Estimated costs of the vacuum system including vessels, pumping, valves, gauges and controls and other mechanical structures.

Item	Unit Cost($)	# Units	Cost(K$)
Trigger			75
DAQ			100
Transient Digitizers	500	2900	1450
Trigger/DAQ Subtotal			1625

Table 16: Estimated costs of the trigger and DAQ systems.

Item	Unit Cost($)	# Units	Cost(K$)
Photubes and bases	300	200	60
H.V. and cables	100	200	20
Electronics	100	200	20
Materials			150
Catcher/DAQ Subtotal			250

Table 17: Estimated costs of the beam catcher and downstream veto systems.

[2] L. Littenberg and G. Valencia, *Ann. Rev. Nucl. Part. Sci.* **43**, 729 (1993); B. Winstein and L. Wolfenstein, *Rev. Mod. Phys.* **65**, 1113 (1993); J.L. Ritchie and S.G. Wojcicki, *Rev. Mod. Phys.* **65**, 1149 (1993); G. Buchalla, A.J. Buras and M.E. Lautenbacher, FERMILAB-PUB-95/305-T, *Rev. Mod. Phys.*, to br published.

[3] G. Buchalla and A.J. Buras, *Nucl. Phys.* **B400**, 225 (1993).

[4] W.J. Marciano and Z. Parsa, *Phys. Rev.* **D53**, R1 (1996).

[5] G. Buchalla and A.J. Buras, *Nucl. Phys.* **B412**, 106 (1994).

[6] G. Buchalla and A.J. Buras, in preparation.

[7] M. Gronau, *Phys. Lett.* **B300**, 163 (1993).

[8] A.J. Buras, *Phys. Lett.* **B333**, 476 (1994).

[9] C. Dib, D. London and Y. Nir, *Int. J. Mod. Phys.* **A6**, 1253 (1991).

[10] G. Bélanger, C.G. Geng and P. Turcotte, *Phys. Rev.* **D46**, 2950 (1992).

[11] C.E. Carlson, G.D. Dorata and M. Sher, hep-ph/9606269, to appear in *Phys. Rev.* **D**.

[12] I.I. Bigi and F. Gabbiani, *Nucl. Phys.* **B367**, 3 (1991).

[13] M. Weaver et al., Phys. Rev. Lett. **72**, 3758 (1994).

[14] R. Cappi and C. Steinbach, CERN-PS-OP-81-10, *Particle Accelerator Conference 1981*, 2806.

[15] J. W. Glenn, AGS/AD Technote 426 (1996).

[16] G. Bock, private communication.

[17] Y. Pang, T.J. Schlagel, and S.H. Kahana, *Nucl. Phys.* **A544**, 435c (1992).

[18] R. Wojcik et al., NIM, **A342** (1994) 416.

[19] Yu.Kudenko and O.Mineev, private communication.

[20] M. Chung and S. Margulies, IEEE Trans. on Nucl. Sci., **42** (1995) 323.

[21] K. Hara et al., NIM, **A348** (1994) 139.

[22] O.Dubois et al., NIM, **A368** (1996) 640.

[23] R.Brun, F.Carminati, GEANT Detector Description and Simulation Tool, CERN Program Library Long Writeup W5013, March 1994.

[24] C.Zeitnits and T.A.Gabriel, The GEANT-CALOR interface and benchmark calculations of ZEUS test calorimeter, NIM **A349** (1994) 106.

[25] A. Antonelli, et al., N.I.M. **A354** 352 (1995).

[26] T. S. Virdee, Proc. Sec. Intl. Conf. Caloimetry in H. E. P., ed. A. Ereditato, World Scientific (1991).

[27] R. Wigmans, Proc. Second Intl. Conf. Caloimetry in H. E. P., *op. cit.*.

[28] J. Kouptsidis, R. Banthau, and H. Hartwig, IEEE Trans on Nuclear Science, NS-32 3584(1985).

[29] J.R.J.Bennett, R.J.Elsey and R.W.Malton, Vacuum **43** 531 (1992).

[30] R.J.Roark and W.C.Young, McGraw-Hill.

[31] C. Hauviller, Proc. 1988 EPAC, Rome 1143 (1988).

[32] T. Inagaki, et al., N.I.M. **A359** 478(1995).

[33] B.A. Cole, *et al.*, AGS-Proposal 910, 1995.